A review of abyssal serpentinite geochemistry and geodynamics

Baptiste Debret, Muriel Andreani, Marguerite Godard

Earth-Science Reviews 258 (2024) 104910

Contents lists available at ScienceDirect

Earth-Science Reviews

journal homepage: www.elsevier.com/locate/earscirev

Review Article

A review of abyssal serpentinite geochemistry and geodynamics

Baptiste Debret [a,*], Muriel Andreani [b,c], Marguerite Godard [d]

[a] Institut de physique du globe de Paris, Université Paris Cité, CNRS, Paris, France
[b] Université Lyon 1, CNRS UMR5276, ENS de Lyon, LGL-TPE, 2 rue Raphael Dubois, 69622 Villeurbanne Cedex, France
[c] Institut Universitaire de France
[d] Géosciences Montpellier, CNRS, Montpellier University, 34095 Montpellier, France

ARTICLE INFO

Keywords:
Abyssal serpentinites
Geochemistry
Geodynamical setting
Tectonic context

ABSTRACT

The formation of abyssal serpentinites leads to deep changes of the oceanic lithosphere rheology and geochemistry, hence playing a key role on geodynamic and geochemical cycles. Here we review and discuss the geochemical diversity of serpentinites collected on abyssal floors (i.e., abyssal serpentinites) from different geodynamical settings, namely passive margin, forearc and oceanic spreading ridges. We further divided abyssal serpentinites from spreading ridges according to the tectonic contexts in which they were exhumed, differentiating slow-spreading centres (exhumed within the axial valleys and at oceanic detachments), ultra-slow spreading centres (from amagmatic axial valleys and smooth seafloor), fast spreading axis (mostly from deeps) and large transform faults (all spreading rates).

The major and trace element composition of abyssal serpentinites is first controlled by melt extraction and melt/rock interaction processes occurring prior to serpentinization. Slow-, fast- spreading ridges and forearc serpentinites are distinguished by low Al_2O_3/SiO_2 ratios and depleted REE signatures when compared to abyssal serpentinites recovered from ultra-slow spreading ridges, transform faults and passive margins, where magmatic extraction is likely more limited or/and melt/rock reaction prominent. Ultra-slow spreading ridge serpentinites have high $Fe^{3+}/\sum Fe$ when compared to passive margin and forearc serpentinites, while slow spreading ridge and transform fault serpentinites have intermediate $Fe^{3+}/\sum Fe$, close to that of magnetite. This distribution is correlated with MgO/SiO_2 ratios, suggesting that high MgO contents could thwart Fe oxidation, and thus H_2 production, in abyssal environments.

The presence of mafic units at depth affects the chemical properties (e.g., sulfur activity [aH_2S], oxygen fugacity (fO_2)) of the serpentinizing fluids leading to contrasting enrichments of redox sensitive elements (S, U, Eu, Ce, As, Sb) and metals (Zn, Cu) in abyssal serpentinites. At slow-spreading ridges, the circulation of high aH_2S and low fO_2 fluids, equilibrated with gabbroic rocks, leads to the formation of serpentinites with pronounced Eu anomalies, enrichments of LREE over M-HREE and of As over Sb, and to the storage of metal (Zn, Cu) and sulfide in serpentinites. In contrast, at ultra-slow spreading ridges and at transform faults, the absence of an active magmatic system limits changes in seawater composition prior to serpentinization. The oxidizing conditions favours Ce(IV) (Ce anomalies on REE patterns), and the preferential mobility of Sb(V) over Sb(III) (coupled behaviour between Sb and As), as well as the storage of sulfate over sulfides in rocks. Fast spreading ridge serpentinites present both features with samples having negative Ce anomaly (Ce (IV)) and others with positive Eu* (Eu (II)). Fluid mobile (FME) and non-redox sensitive elements (e.g., Cs, Ba, Rb, B or Li) in abyssal serpentinites are homogeneous at oceanic spreading ridges. Both passive margin and forearc serpentinites are free of Ce anomalies and only few forearc samples display Eu anomalies with moderate LREE enrichments. The forearc serpentinites appear as a geochemical endmember. There, the influence of slab-derived fluids enhances the formation of FME-rich serpentinites having a strong affinity with CO_2-rich sediment-derived fluids (i.e., enrichments in Cs and As relative to Rb and Sb respectively).

* Corresponding author.
E-mail address: debret@ipgp.fr (B. Debret).

https://doi.org/10.1016/j.earscirev.2024.104910
Received 29 March 2024; Received in revised form 4 August 2024; Accepted 27 August 2024
Available online 30 August 2024

1. Introduction

Serpentinites are of particular importance for global geochemical cycles. They regulate chemical exchanges between Earth's main reservoirs, from mid-oceanic ridges during seawater percolation within the lithosphere to subduction zones during slab dehydration and recycling to the deep mantle. Over the last decades, serpentinites have received much attention, especially in subduction zones where many reviews have established their elemental and redox budgets (Cannaò and Malaspina, 2018; Deschamps et al., 2013; Hattori and Guillot, 2007; Pettke and Bretscher, 2022; Scambelluri et al., 2019), emphasizing their importance for arc magma composition (e.g., Debret and Sverjensky, 2017; Scambelluri and Tonarini, 2012; Zhang et al., 2021) and deep mantle chemical evolution over geological times (Bouilhol et al., 2022; Duncan and Dasgupta, 2017; Eguchi et al., 2020). In contrast to the large number of high-quality geochemical studies of subduction-related serpentinized peridotites, less geochemical studies focused on abyssal serpentinized peridotites (see section 2 for a review of available data). Most studies have assessed the role of pre-existing mantle composition, partial melting and/or melt-rock interaction processes affecting abyssal peridotite composition prior to their exhumation and serpentinization (see for example the reviews of Bodinier and Godard, 2013; Niu, 2004 or Warren, 2016), while geochemical studies of abyssal serpentinites are limited to regional observations (e.g., Paulick et al., 2006; Vils et al., 2009). Hence, there is a significant knowledge gap regarding the role of the serpentinization processes on the geochemical budget of abyssal peridotites worldwide.

The serpentinization process principally leads to the recrystallization of anhydrous mantle minerals, such as olivine [$(Mg,Fe)_2SiO_4$] and orthopyroxene [$MgSiO_3$], into serpentine [$(Mg,Fe,Ni)_3Si_2O_5(OH)_4$], a phyllosilicate integrating up to 13 wt% of water in its structure, as well as variable amounts of brucite [$(Mg,Fe)(OH)_2$] and magnetite [Fe_3O_4]. This process is particularly efficient near major tectonic structures, such as extensive faults (normal or oceanic detachment faults) or transform faults that serve as major fluid paths to the deep lithosphere (see Mével, 2003 for comprehensive reviews of abyssal peridotite serpentinization at mid-ocean ridges). Abyssal serpentinites were principally recognized at slow and ultra-slow spreading ridges where they represent a major component of the oceanic crust (Cannat, 1995; Sauter et al., 2013), but also at fast-spreading ones although their presence on the seafloor is scarce (Mével and Stamoudi, 1996). Serpentinites also occur in abundance in other abyssal settings. They were documented at passive margins (e.g., Iberia margin), where they result from mantle exhumation due to crustal thinning during the initial rifting stages (Beslier et al., 1993; Boillot et al., 1980). Active margins such as the Tonga or Mariana trenches also expose serpentinites (Ewans and Hawkins, 1979; Ficher and Engel, 1969) that are clearly associated with subduction related processes and are thought to result from mantle wedge exhumation (Fryer, 2012). In all these abyssal geodynamical settings and tectonic contexts, the structure and lithology of the oceanic lithosphere, as well as the thermal regimes influence serpentinizing conditions, fluid composition, metamorphic reaction pathways and therefore are expected to deeply impact the chemistry of serpentinites. In particular, the serpentinization is associated with reducing conditions, as a consequence of H_2 production due to the oxidation of Fe^{2+} to Fe^{3+} in the host rock by water (Andreani et al., 2013; McCollom and Bach, 2009; Mével, 2003). However, large variations of fO_2 or extensive variables (e.g., aH_2S or $aSiO_2$) are expected across serpentinization settings influencing the stability of redox phases, such as sulfide/sulfate, carbonaceous compounds/carbonates, Fe-bearing opaques, and therefore the redox budget of abyssal serpentinites worldwide.

This review concentrates on the geochemistry of serpentinites collected on abyssal floors by dredging, submersible and drilling during oceanographic expeditions in the main geodynamical settings described hereafter, i.e., oceanic spreading ridges, passive margins and forearcs. Ocean ridge settings were further divided according to the tectonic contexts in which the serpentinites were sampled, i.e., slow-spreading centres, ultra-slow spreading centres, fast spreading axis and large transform faults (all spreading rates). This classification allows to decipher the influence of the local tectono-magmatic framework on fluid geochemistry and serpentinite composition. The aim is to establish key geochemical characteristics of each serpentinization setting and context, providing a robust database for future oceanographic expeditions and for deciphering the origin of the serpentinization in orogenic contexts. We first review the main characteristics of serpentinization conditions in each geodynamical setting and tectonic context where abyssal serpentinites occur. Then, on the basis of a comprehensive review of the data available in the literature and of new geochemical data, we compare the major, volatile, trace and stable isotope (S, C, Fe, Zn and Cu) signatures of abyssal serpentinites. Finally, we discuss the role of serpentinization processes on the distribution of volatile and redox sensitive elements within the oceanic lithosphere and highlight the main geochemical heterogeneities among the different geodynamical settings and tectonic contexts.

2. Geodynamical setting and tectonic context

We describe here the morphology, the tectonic, magmatic and geophysical characteristics, and the conditions of serpentinization associated with each geodynamical setting. Each setting is expected to influence the conditions (e.g., pressure, temperature, oxygen fugacity) and the nature (e.g., composition, pH, activity, source) of the serpentinizing fluids, hence having a first order control on abyssal serpentinite mineralogy and geochemistry. The Fig. 1 locates the samples compiled in this work.

2.1. Mid-oceanic ridges

We grouped abyssal serpentinites from mid-oceanic ridges according to their geographical proximity with tectonic structures, namely, slow-spreading centres (abyssal serpentinites exhumed within the axial

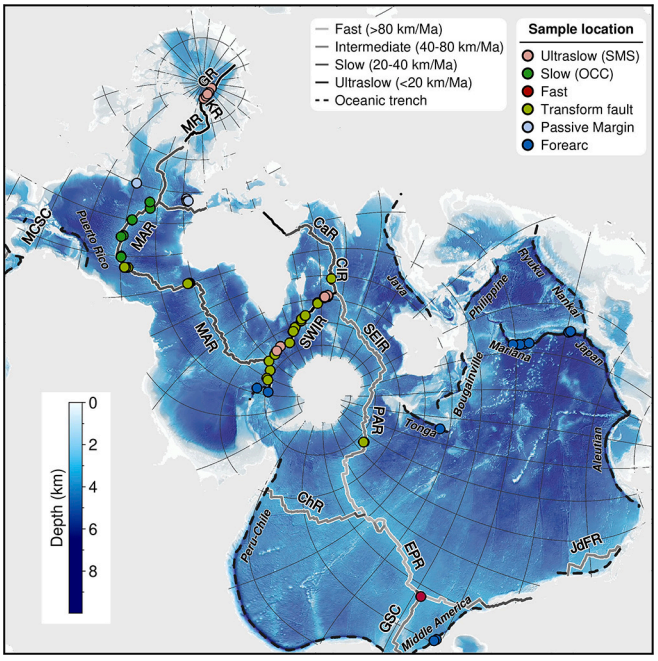

Fig. 1. Spilhaus projection map of abyssal serpentinites global distribution. The map displays the location of geodynamical settings and tectonic contexts in which abyssal serpentinites with geochemical published data were collected (locations and references are display in Electronic Appendix). It does not reflect the entire collection of abyssal serpentinites worldwide. The projection was created by the ArcGIS Pro 2.5 software (Chen et al., 2023).

valleys and at oceanic detachments), ultra-slow spreading centres (abyssal serpentinites from amagmatic axial valleys and smooth seafloor), fast spreading axis (mostly from deeps) and transform faults (all spreading rates).

2.1.1. Slow-spreading ridges

At slow-spreading ridges, serpentinized peridotites were mainly sampled at segments ends, along with limited volcanic rocks and variable amounts of deep magmatic rocks exhumed through long-lasting detachment faults (thereafter referred as oceanic detachments) that root at depths of up to ~10 km below seafloor (b.s.f.). These structures can form corrugated, dome-shaped massifs, recognizable on bathymetric images and known as oceanic core complexes (OCC; Escartin et al., 2008; Escartin and Canales, 2011; Ildefonse et al., 2007; MacLeod et al., 2009; Tucholke et al., 1998). Detachment faulting leads to the asymmetric accretion of a heterogeneous oceanic lithosphere made of peridotites embedding not negligible proportions of gabbroic rocks (~50 % in average, Tucholke et al., 2008).

The study of rock and microseismicity at oceanic detachments exposed along the Mid-Atlantic ridge (MAR) reveal brittle deformation ($T < 750$ °C for the oceanic lithosphere; Searle and Escartín, 2004) and possible water penetration down to ~6–10 km b.s.f. (Craig and Parnell-Turner, 2017; Dusunur et al., 2009; Grevemeyer et al., 2019; Miranda and John, 2010; Parnell-Turner et al., 2021; Picazo et al., 2012). However, seismic profiles suggest that detectable serpentinization (>5 %) associated with oceanic detachments progressively decreases with depth and remains restricted to the first ~4 km b.s.f., (Blackman et al., 2009; Bown and White, 1994; Canales et al., 2000; Dunn et al., 2017).

Petrographic and isotopic studies of serpentinites indicate that their alteration starts below ~500 °C and that the main serpentinization stage occurs near 300 °C where olivine is most reactive, with minor episodes at lower temperature (Agrinier and Cannat, 1997; Andreani et al., 2014; McCaig et al., 2010; Rouméjon et al., 2018). As predicted by thermodynamic calculations and experimental results, the dominant forms of serpentine near 300 °C are lizardite and chrysotile polymorphs with abundant magnetite (Andreani et al., 2007; Bach et al., 2004; Bonnemains et al., 2016; Klein et al., 2014; Maffione et al., 2014; Mével, 2003). Rare antigorite has been observed in areas moderately enriched in Si (Rouméjon et al., 2019).

Data on abyssal serpentinites from oceanic detachments at slow-spreading ridges regroup samples that were collected along the axial valley of the MAR and at oceanic detachment (Fig. 1). The database includes abyssal serpentinites sampled by drilling to the north and south of the MAR 15°20′ fracture zone (Alt et al., 2007; Jöns et al., 2010; Kodolányi et al., 2012; Mothersole et al., 2017; Paulick et al., 2006; Regelous et al., 2016), within the western fault scarp bounding the MARK area (Alt and Shanks, 2003; Andreani et al., 2013; Day et al., 2017; Debret et al., 2018; Regelous et al., 2016, this study) and the west flank of the North Central Atlantic ridge (Regelous et al., 2016), by TV-guided grab at the massif hosting Logachev hydrothermal field on the eastern rift valley flank of the MAR (Augustin et al., 2008, 2012), and by drilling, dredging and/or diving at OCCs including the Rainbow (Andreani et al., 2014; Debret et al., 2018) and the Atlantis massifs (Delacour et al., 2008a, 2008b; Regelous et al., 2016; Ternieten et al., 2021; Whattam et al., 2022; see location in Electronic Appendix).

2.1.2. The amagmatic Smooth seafloor (SMS) at ultra-slow spreading ridges

Along ultraslow-spreading ridges (full extension rate < 3 cm/yr), serpentinized peridotites can represent up to 25 % of the accreted lithosphere (Grevemeyer et al., 2018; Hayman et al., 2011; Sauter and Cannat, 2010). "Smooth-seafloor" (SMS), only identified at ultraslow-spreading ridges, is an additional structural domain capable of exhuming peridotites. It is characterized by the absence of corrugations along exhumed section, and the lack of volcanic rifts, giving a smooth aspect to the seafloor (Cannat et al., 2006; Sauter et al., 2013). This domain comprises abundant peridotites with rare basalts and virtually no gabbroic bodies, attesting of a very limited magmatic activity (Cannat et al., 2008; Tucholke et al., 2008).

According to the depth of micro-earthquakes, the brittle-to-ductile transition at ultra-slow spreading ridges may extend to 10–17 km depth (Grevemeyer et al., 2019). This could highlight a deep serpentinization of the oceanic lithosphere, potentially deeper to that expected at slow-spreading ridges. However, such a result contrasts with the depth of serpentinization as estimated from seismic profiles, which suggest that serpentinization occurs to a maximum depth of 5 km b.s.f. (Corbalán et al., 2021), i.e. similar to slow-spreading contexts.

Serpentinization of the lithosphere exposed at SMS dominantly occurs at the same range of T as slow-spreading settings, between 200 and 300 °C, as estimated by oxygen isotopes (Rouméjon et al., 2014). But the fluid composition differs, as it did not undergo exchanges with magmatic bodies and rather displays a composition closer to seawater, and probably alkaline (Rouméjon et al., 2014). The petrographic characteristics of serpentinites generated at SMS are similar to that described at slow-spreading ridges, with mineralogical assemblages dominated by lizardite, chrysotile, rare antigorite and magnetite (Rouméjon et al., 2014). So far, only low-T hydrothermal activities, similar to Lost City (Kelley et al., 2005), have been described on smooth-seafloor regions (Old City; Lecoeuvre et al., 2021).

Data of abyssal serpentinites from ultra-slow spreading ridges regroup samples dredged along the South West Indian Ridge on amagmatic segments, between 60 and 65°E (Dessimoulie, 2019; Dessimoulie et al., 2020; Niu, 2004; Rouméjon, 2014; Zeng et al., 2012) and between 9 and 16°E (Craddock et al., 2013; Day et al., 2017), and along the sparsely magmatic zone of the Gakkel ridge (Craddock et al., 2013; Day et al., 2017; Liu et al., 2019; Regelous et al., 2016; see location in Electronic Appendix).

2.1.3. Fast spreading ridges

The abundant magmatic activity at fast spreading ridges results in a thick mafic oceanic crust that hampers the exhumation of mantle rocks, while temperatures near the axis may be too high to allow an extensive serpentinization of the mantle. Hence, whether or not the mantle is serpentinized below this mafic crust remains an open question and serpentinization might therefore be limited to off-axis processes. Study of analogous ophiolites usually favours a main serpentinization stage during the obduction process (Barnes et al., 1978), while relict oceanic serpentinization may have been fully overprinted. Hence, exposures of peridotites at fast spreading ridges are scarce, and their occurrence required specific tectonic contexts (i.e., deeps) where the thick oceanic crust was deeply dissected by normal faulting (e.g., Hess Deep) allowing access to the lithospheric mantle, mainly at the tip of ridge propagators.

Investigations of fast-spreading ridge serpentinites show that the temperature of serpentinization ranges between 200 and 350 °C (Agrinier et al., 1995), similar to that record at slow- and ultra-slow spreading ridges and probably reflecting fluid/rock interaction during peridotite exhumation along deeps. Recovered abyssal serpentinites are closely associated with gabbroic rocks and display evidences for melt impregnation processes (e.g., clinopyroxene-spinel intergrowths and Al enrichment in ferromagnesian minerals, (Arai and Matsukage, 1996; Edwards and Malpas, 1996). The mineralogy of abyssal serpentinites along deeps is quite simple and dominated by lizardite/chrysotile and magnetite intergrowths forming the classical mesh and bastite textures (Mével and Stamoudi, 1996).

Data of abyssal serpentinites from deeps along fast spreading ridges are limited to the drilling of the Hess Deep area in the East Pacific Rise (Alt and Shanks, 1998; Kodolányi et al., 2012; Paquet et al., 2022; Regelous et al., 2016), see location in Electronic Appendix).

2.1.4. Oceanic Transform faults

Oceanic Transform faults (OTF) are widespread along fast, slow and ultra-slow spreading ridges. The length of the transform fault is highly

variable, from ~10 km up to 1000 km (e.g., Romanche, MAR), so is the width which varies from 1 to >30 km (Bonatti and Crane, 1984). OTF are usually composed of a deep valley flanked on both sides by two prominent ridges. It is expected that the flanks might be influenced by tectonic reworking of pre-existing structure (i.e., serpentinite hydrated at the ridge and exposed along the fault), while the centre of the OTF should exhumed deep lithospheric rocks. Serpentinized peridotites are abundant, while mafic rocks are scarce, within transform fault zones. These rocks are thought to be exhumed by transtension or transpression movement accommodating the changing geometry of ridge-transform intersection (Bonatti et al., 2005, 1994).

Geophysical observations indicate gravity anomalies (Gregg et al., 2007; Pickle et al., 2009) and low seismic wave velocities compared to the surrounding lithosphere (Froment et al., 2014; Roland et al., 2012), advocating for extensive serpentinization of the mantle along OTF. Low-velocity anomalies down to 9 km suggest that the depth of serpentinization might exceed that reported along spreading centres (Gregory et al., 2021). Based on numerical models, relatively low amount of magmatic rocks (<10 %) are expected at depth within OTF (Bonatti et al., 2001).

OTF serpentinized peridotites can be highly deformed (e.g., mylonitic textures) and record a large range of hydration temperatures, from amphibole-rich mylonites indicative of fracturing and fluid flow up to 850–875 °C, to lizardite and chrysotile bearing serpentinites equilibrated at ~120 °C according to oxygen isotopes (Boschi et al., 2013; Prigent et al., 2020). Most of OTF serpentinites display $^{87}Sr/^{86}Sr$ ratios close to that of seawater, suggesting intense interactions with seawater-derived fluids that had negligible interactions with surrounding magmatic rocks or sediments, in agreement with Cl and B isotopic data (Boschi et al., 2013).

Data of transform fault serpentinites include both samples taken away from the spreading axis and samples from the central fault area. They were all recovered by dredges or dives from the Vema Lithospheric Section (Boschi et al., 2013), the Romanche OTF (this study) and the Ascension 2B (Regelous et al., 2016) along the MAR, the Unditsev OTF crossing the Pacific Antarctic Ridge (Niu, 2004; Paquet et al., 2022) and numerous transform faults along the American Antarctic Ridge, the South West and Central Indian Ridge compiled by Niu (2004), Liu et al. (2019) and Day et al. (2017) (see locations in Electronic Appendix).

2.2. Forearc

Serpentinization of the forearc area is related to slab devolatilization and mantle wedge metasomatism by slab derived fluids, rather than seawater percolation to depth (Hyndman and Peacock, 2003). The most studied examples of forearc mantle hydration and serpentinization include serpentinite mud volcanoes in the Mariana and Izu-Bonin forearcs (Fryer, 1996). There, the exhumation of serpentinite muds containing abundant clasts of the forearc mantle is linked to large normal fault systems affecting the first kilometres of the oceanic crust (Fryer, 2012). These faults result from the increasing curvature of the forearc and the rollback eastward of the Pacific Plate (Fryer et al., 1999). They allow fluids originating from the subduction channel to percolate through the forearc mantle and erupt to form serpentinite mud volcanoes of up to 50 km in diameter and 2.5 km in height (e.g., Asut Tesoru).

The size and the serpentinization degree of the forearc area is mainly controlled by isotherm distributions (Abers et al., 2017) and is highly variable from one subduction to another. Geophysical observations suggest that the forearc mantle may commonly be ~20 % serpentinized with, locally, serpentinization degree reaching 50 % (Hyndman and Peacock, 2003). It is inferred that the serpentinized forearc mantle wedge never excess 600–700 °C, the upper limit of antigorite stability field (Ulmer and Trommsdorff, 1995), limiting its depth to approximately 80 km.

Investigations of serpentinite clasts recovered in serpentinite mud volcanoes show that the serpentinization temperature ranges between 180 and 420 °C, based on oxygen isotopes measurements (Alt and Shanks, 2006; Debret et al., 2019). The clasts display highly variable mineralogical assemblages, from Fe-rich lizardite and brucite when serpentinization occurs at low temperature nearby the seafloor (< 200 °C), to abundant antigorite, Fe-poor brucite and magnetite when serpentinization occurs close to the slab interface at higher temperature (>250 °C) and depth of more than 15 km (Debret et al., 2019).

Data of forearc serpentinites correspond to samples dredged from the Guatemala (Geldmacher et al., 2008; Kodolányi et al., 2012), the Tonga (Birner et al., 2017; Day and Brown, 2021) and the Sandwich (Pearce et al., 2000) subduction zones, and drilled samples from the Mariana subduction zone (Alt and Shanks, 2006; Debret et al., 2019, 2020, 2022; Kodolányi et al., 2012; Parkinson and Pearce, 1998; Savov et al., 2005a, 2005b, 2007 – excluding serpentinite muds; see location in Electronic Appendix).

2.3. Passive margins

The formation of passive margin serpentinites is attributed to the rifting of the continent that brought up deep continental mantle lithosphere close to the surface. The serpentinization can occur by the exhumation of ultramafic rocks to the seafloor and/or by crustal-scale brittle faulting accompanying continental rifting and creating fluid pathways for seawater to reach and react with the cold lithospheric mantle (Bayrakci et al., 2016; Pérez-Gussinyé and Reston, 2001; Rüpke et al., 2013).

The depth of serpentinization at passive margin is mainly controlled by the thickness of the continental crust and the occurrence of normal faulting. The seismic velocity profiles of magma-poor area are comparable to that described at ultra-slow and slow-spreading mid-ocean ridges, with a depth of serpentinization estimated nearby ~5 km (Minshull, 2009). However, large heterogeneities and lateral variations of serpentinization depth (up to 2 km) are reported along passive margins, with the serpentinization process being largely concentrated beneath the hanging wall of normal faults (Bayrakci et al., 2016).

Temperature of serpentinization as estimated by oxygen isotopes are usually <200 °C (Agrinier et al., 1988; Klein et al., 2014; Schwarzenbach et al., 2013; Tichadou et al., 2021), i.e., lower than those estimated in other geodynamical settings. Petro-geochemical investigation of passive margin serpentinites show that they contain higher modal amounts of pyroxene than peridotite at MOR (Hébert et al., 2001; Tichadou et al., 2021). The serpentinites are characterized by small magnetite amounts (Albers et al., 2021; Bonnemains et al., 2016; Klein et al., 2014), in agreement with the low T of serpentinization (Seyfried Jr et al., 2007) and the absence of magnetic anomalies in this setting (Boillot et al., 1980). Serpentine usually form pervasive textures such as mesh and bastite with a strong yellow colour attributed to the iron enrichment of phyllosilicates.

Data of passive margin serpentinites include samples drilled at the Iberian abyssal plain (Albers et al., 2021; Alt and Shanks, 1998; Kodolányi et al., 2012; Milliken et al., 1996; Schwarzenbach et al., 2012, 2013; Seifert and Brunotte, 1996) and the Newfoundland passive margin (Kodolányi et al., 2012; see location in Electronic Appendix).

3. Materials and methods

3.1. Data compilation

The compilation of abyssal serpentinite compositions and locations is reported in Electronic Appendix A. The database includes data from the literature and new data. It is divided into five tables regrouping different type of measurements: Fe, S and C redox (Electronic Appendix Tables S1–3), major and trace elements (Electronic Appendix Table S4) and Fe-Zn-Cu isotopes (Electronic Appendix Table S5). This division was necessary in order to present, compare and discuss coherent datasets.

The Electronic Appendix Table S4 is an implementation of Deschamps et al. (2013) and Peters et al. (2017) compilations. Data from abyssal settings were compared to serpentinized peridotites displaying various degrees of serpentinization from on land (meta-)ophiolites in the section 4.1. These serpentinized peridotites regroup samples from Pindos (Bonnemains et al., 2016), Oman (Godard et al., 2000), the Chenaillet (Debret et al., 2014), the Apennines (Schwarzenbach et al., 2013) and New Caledonia (Mothersole et al., 2017) (meta-)ophiolites.

Abyssal serpentinites can form after all kind of ultramafic rocks, including MgO-rich mafic rocks (e.g., troctolite) or CaO- and SiO_2 rich pyroxenites, and be affected by late low temperature metasomatism or weathering (e.g., carbonatation, chloritisation or clay weathering) overprinting the primary geochemical signature of the serpentinization process. In order to consider serpentinites formed from peridotites only, we assume that Al_2O_3/SiO_2 ratios are poorly affected by the serpentinization processes, as proposed by Paulick et al. (2006) and as discussed in section 5.1, and that this ratio must overlap that of mantle peridotites which is inferior to 0.12 (Bodinier and Godard, 2013). Similarly, we assumed that Ca is highly mobile in fluids during serpentinization and that this element is not incorporated within serpentine structure or other minerals associated with the serpentinization process (e.g., magnetite, brucite, talc). We therefore consider that the CaO contents of serpentinites cannot exceed that of mantle peridotites, the latter being inferior to 4 wt% (Bodinier and Godard, 2013). Finally, we excluded all samples reported as serpentinites but displaying abnormally high SiO_2 contents (i.e., superior to 50 w%). When major element chemistry was non-available, all samples that were not described as serpentinites or serpentinized peridotites were discarded (this is particularly relevant for Electronic Appendix Tables S2 and S3). Similarly, samples described as metasomatized or weathered were also discarded.

The non-traditional isotope dataset (Electronic Appendix Table S5) rules out analyses for which no specific procedure was implement to dissolve refractory phases, such as spinel, which can be abundant in serpentinites. Indeed, spinels commonly display high [Zn] and $\delta^{66}Zn$ values relative to mantle silicates and sulfides (Ducher et al., 2016; Wang et al., 2017), the incomplete dissolution of spinel during serpentinite dissolution will lead to apparently light $\delta^{66}Zn$ and low [Zn] relative to mantle values (e.g., Pons et al., 2011).

3.2. Acquisition of new data

A lack of dataset was observed in the Central and South Atlantic Ocean. To complement previous studies, a suite of abyssal serpentinites from the Romanche transform fault (SMARTIES cruise, Maia et al., 2019)) were analysed for major and trace elements. Similarly, we complement previous dataset from the MARK area (ODP Leg 153, site 920) and the Mariana forearc (IODP exp. 366) with, respectively, new trace elements and Zn stable isotope analyses.

3.2.1. Major elements

Major elements (SiO_2, Al_2O_3, Fe_2O_3, MnO, MgO, CaO, Na_2O, K_2O, TiO_2) were analysed by Inductively Coupled Plasma Optical Emission Spectrometry (Thermo ICP-OES Icap 6500) at the SARM (Service d'Analyses des Roches et des Minéraux Nancy, France – Electronic Appendix Table S4). Sample digestions were performed on $LiBO_2$ fluxed fusions following the procedures described by Carignan et al. (2001). The long-term reproducibility of the SARM standard (UB-N serpentinite standard from the Centre de Recherches Pétrographiques et Géochimiques (CRPG) of Nancy, France) is better than 2 % for major elements (https://sarm.cnrs.fr). Additional FeO titration of bulk-rock samples were performed at the SARM. These analyses were done by automatic titration at the equivalent point with potassium dichromate after dissolution of the sample in a HF/H_2SO_4 mixture, in the presence of H_3BO_3 and H_3PO_4. Subsequently, $Fe^{3+}/\Sigma Fe$ ratios were calculated from the measured $Fe_2O_3^{Tot}$ and FeO^{Tot} values.

3.2.2. Trace elements

Trace elements (Li, Sc, Ti, V, Co, Ni, Cu, Zn, As, Rb, Sr, Y, Zr, Nb, Sb, Cs, Ba, Rare Earth Elements (REE), Hf, Ta, Pb, Th, and U) were analysed at the University Montpellier (France) on a quadrupole VG-PQ2 ICP-MS following the procedure described in Godard et al. (2000). The method involves dissolution of 100 mg aliquots in a $HF/HClO_4$ mixture and 1000× dilution. In and Bi were used as internal standards during ICP-MS measurements. Elemental concentrations were determined by external calibration using multi-element standard solutions (Merck) except for Nb and Ta. To avoid memory effects due to the introduction of concentrated Nb—Ta solutions in the instrument, Nb and Ta concentrations were determined by using, respectively, Zr and Hf as internal standards. This technique is an adaptation to ICP-MS analysis of the surrogate-calibration method described by Jochum et al. (1990) for the determination of Nb by spark-source mass spectrometry. Accuracy was assessed using certified rock materials, serpentinite UB-N and peridotites JP-1, DTS-1 and DTS-2b (see standard values on Electronic Appendix). Additional boron concentrations were measured by spectrophotometric determination using an Agilent CARY60 at the SARM. For boron, the long-term reproducibility was between 10 % and 20 % at 100 ppm and 10 ppm, respectively (Och and Shields-Zhou, 2012).

3.2.3. Zinc stable isotopes

Zinc stable isotopes ($\delta^{66}Zn$) were analysed at the Université Libre de Bruxelles (Belgium) on a Nu Plasma II Multi-Collector-Inductively Coupled Plasma-Mass Spectrometer (MC-ICP-MS Nu Instruments, Ltd.). About 100 mg of powdered samples were dissolved using a 1:1 mix of concentrated HF and HCl in Parr bombs at 160 °C in an oven for 5 days. These were then further attacked with aqua regia, a 1:3 mix of concentrated HNO_3 and HCl for 3 days at 130 °C. Finally, samples were brought into solution in 6 M HCl prior to column chemistry. Quantitative purification of Zn was achieved by chromatographic exchange, using 1 ml of AG1-x8 (200–400 mesh) and 0.4 × 7 cm Teflon columns, following the procedure developed by (Sossi et al., 2015). The analyses were performed in wet plasma mode following the procedure of Debret et al. (2018). Instrumental mass bias was corrected by sample-standard bracketing and external normalization (Cu-doping technique). Each sample was bracketed by two analyses of a standard (Zn in-house standard). The $\delta^{66}Zn$ isotope composition of the samples is presented as a delta value in permil notation relative to the JMC-Lyon isotopic standard. During data acquisition, IRMM-3702 ($\delta^{66}Zn = 0.28 \pm 0.03$ ‰; $\delta^{68}Zn = 0.59 \pm 0.03$ ‰, $n = 21$) and reference materials (BHVO-2 basalt, JP-1 peridotite and PCC-1 peridotite) were processed through columns and analysed for $\delta^{66}Zn$. Reference material data are displayed in Electronic Appendix and are in good agreement with previous studies.

4. Volatile and redox sensitive element (H_2O, Fe, S and C) storage during abyssal serpentinization

4.1. Interplays between water and iron

One of the major consequences of the serpentinization process is the storage of structural water (OH bounds) in serpentinized peridotites. In absence of a significant modal amount of carbon- and sulfur-bearing phases (e.g., calcite or pyrite), it is often considered that the loss on ignition (LOI) of abyssal serpentinites is a good approximation of their water content and, hence, to their serpentinization degree. The contribution of Fe^{2+} oxidation is neglected, as it has little effects on LOI values (maximum of ~0.8 wt%).

Most abyssal serpentinites display high LOI (> 10 wt%; Fig. 2) close to the water content of serpentine minerals (~ 13 wt%), which is coherent with the high serpentinization degree and the dominance of serpentine minerals observed in thin sections (Mével, 2003). This high degree of serpentinization is attributed to a sampling bias, as abyssal serpentinites are exclusively sampled at, or near, the seafloor (< 1.5 km

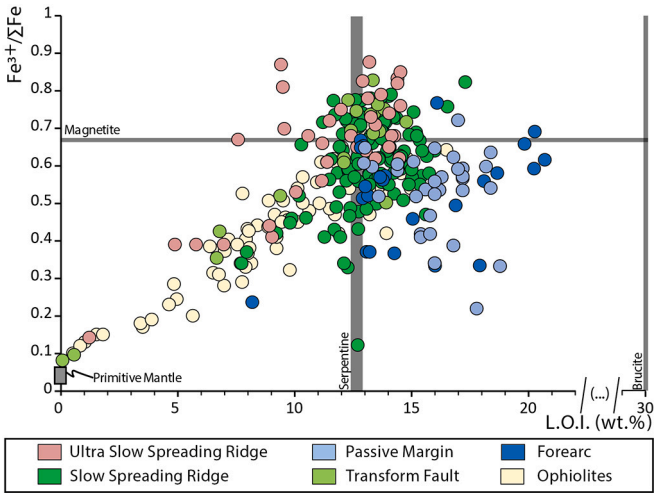

Fig. 2. Iron redox state and water contents in abyssal serpentinites. L.O.I. (Loss On Ignition, in wt%) versus $Fe^{3+}/\sum Fe$ in bulk rock serpentinized peridotites (dataset used is from Electronic Appendix Table S1). Primitive mantle value is from Canil et al. (1994).

depth), hence limiting the access to deep lithospheric levels where the serpentinization degree is expected to significantly decrease. This is confirmed by geochemical data from on-land ophiolites where serpentinites display a decreasing serpentinization degree from paleo-seafloor to paleo-Moho (Debret et al., 2013b; Guillot et al., 2015) and overall a larger range of LOI relative to abyssal serpentinites.

The serpentinization of peridotite is commonly associated with the oxidation of iron, from ferrous (Fe^{2+}) iron mainly stored in olivine to ferric (Fe^{3+}) iron stored in newly formed minerals, dominantly magnetite at high temperature (~300 °C) and Fe^{3+}-serpentine at lower temperature (< 200 °C) (Andreani et al., 2013; Bonnemains et al., 2016; Evans, 2008; Klein et al., 2014; Seyfried Jr et al., 2007). The redox balance involves the liberation of molecular hydrogen according to the simplified reaction:

$$2FeO + H_2O_{(aq)} = Fe_2O_3 + H_{2(aq)} \quad (1)$$

Reaction pathways controlling iron distribution and oxidation, and H_2 production, are complex and not well understood yet. It is notably affected by the precipitation and/or dissolution of secondary minerals (e.g., brucite, sulfide and/or Ni-alloys; Albers et al., 2021; Evans, 2008; Frost and Beard, 2007; Jones et al., 2010; Klein and Bach, 2009; Martin and Fyfe, 1970; McCollom et al., 2020; Pens et al., 2016; Tichadou et al., 2021). From a geochemical perspective, the coupled processes of water storage and iron oxidation are well illustrated by a positive correlation between LOI and $Fe^{3+}/\Sigma Fe$ ratio in serpentinized peridotites (Fig. 2). Some analyses, especially at ultra-slow spreading ridges, have higher $Fe^{3+}/\Sigma Fe$ ratios than magnetite, highlighting the role of Fe^{3+}-rich serpentine minerals and/or late accessory phases (e.g., hematite or goethite; Dessimoulie et al., 2020). Above 10 wt% LOI, the correlation between LOI and $Fe^{3+}/\Sigma Fe$ dies down, the $Fe^{3+}/\Sigma Fe$ ratios range from 0.3 to 0.8 and are not correlated with LOI anymore.

Among the highly serpentinized peridotites, the average $Fe^{3+}/\sum Fe$ values are similar between tectonic contexts, with slow (0.61 ± 0.02, calculated according to 2 s.d. / $\sqrt{(n)}$, s.d., standard deviation, $n = 118$), ultra-slow (0.66 ± 0.05, $n = 37$) spreading ridges and transform fault (0.65 ± 0.06, $n = 18$, excluding two fresh peridotite mylonites) serpentinites having an average value of 0.62 ± 0.02 ($n = 173$). The $Fe^{3+}/\sum Fe$ values plot on the correlation of Fig. 2 showing that the oxidation of iron and H_2 production through water circulation is a ubiquitous process associated with the serpentinization whatever the tectonic setting, and that the main variable that controls this reaction is the serpentinization degree. On Fig. 2, for a given LOI, abyssal serpentinites from ultra-slow spreading ridges display the highest $Fe^{3+}/\sum Fe$ values, with most of the serpentinites having a LOI > 10 wt% standing above the $Fe^{3+}/\Sigma Fe$ ratio of magnetite. This suggest that Fe^{3+}-serpentine carry a significant part of the bulk rock Fe redox budget in this tectonic context.

The $Fe^{3+}/\sum Fe$ values decrease at forearc (0.53 ± 0.05, $n = 24$) and passive margins (0.52 ± 0.03, $n = 52$). This highlight the role of the geodynamical setting influencing metamorphic reaction pathways and therefore iron oxidation and H_2 productivity during the serpentinization process (see also section 5.1). Forearc and passive margin serpentinites stand out off the correlation of Fig. 2. This reflects the role of Fe^{2+}-rich hydrous phases, e.g., Fe-enriched brucite, whose precipitation hampers the oxidation of Fe in these geodynamical settings.

4.2. Sulfur redox state

In mantle peridotites, sulfur is mainly stored in a reduced form (sulfides) and sulfur concentrations vary between 60 and 250 ppm depending on peridotite fertility (Alt and Shanks, 2003). In abyssal serpentinites, the amount and redox state of sulfur are highly variable (Fig. 3a): they range between a sulfate serpentine endmember with low sulfur contents (between 100 and 1500 ppm; Debret et al., 2017), and a sulfide endmember (e.g., pyrite [FeS_2], pyrrhotite [$Fe_{1-x}S$], pentlandite [$(Fe,Ni)_9S_8$]). Overall, abyssal serpentinites display higher sulfur concentrations than mantle peridotites (Fig. 3a), indicating an addition of sulfur during the serpentinization process.

Serpentinites from slow spreading ridges ([S] = 1515 ± 586 ppm; $S^{6+}/\sum S = 0.58 \pm 0.08$, $n = 62$) and passive margin (1771 ± 691 ppm; $S^{6+}/\sum S = 0.59 \pm 0.10$, $n = 35$) display the highest amount of sulfur and sulfides. In contrast, the sulfur redox budget of serpentinites formed at ultra-slow spreading ridges ($S^{6+}/\sum S \sim 1$*; determined by XANES spectroscopy as no geochemical bulk rock study is at that time available, see Debret et al., 2017) or fast spreading axis ([S] = 373 ± 71 ppm; $S^{6+}/\sum S = 0.89 \pm 0.03$, $n = 33$) is mainly carried by sulfate, with significantly lower sulfur concentrations. Among mid-ocean ridge and passive margin serpentinites a negative correlation between sulfur redox state and total concentration is observed. Only forearc serpentinites stand out of this correlation and display highly variable $S^{6+}/\sum S$ and low sulfur concentrations (446 ± 312 ppm; $S^{6+}/\sum S = 0.72 \pm 0.10$, $n = 31$).

Sulfur isotope analyses of sulfides ($\delta^{34}S_{sulfide}$) highlight a multiple origin of this element in abyssal serpentinites (Alt et al., 2007; Delacour et al., 2008a; Schwarzenbach et al., 2012). Their signatures vary between three endmembers (Fig. 3b): mantle (sulfur inherited from the peridotite, $\delta^{34}S = +0.5$ ‰; (Chaussidon et al., 1989), seawater (sulfate, $\delta^{34}S \sim +21$ ‰) and hydrothermal (Alt and Shanks, 2003). Microbial activity can also modify the concentration, redox state and isotope signature of sulfur in abyssal serpentinites(Alt et al., 2007, 2013; Alt and Shanks, 1998). The impact of microbial-dominated systems on sulfur isotopic behaviour was described at the Hess Deep site and on the Iberia Abyssal Plain (Alt and Shanks, 1998; Schwarzenbach et al., 2012).

The stability of mantle sulfides, sulfate-bearing serpentine and hydrothermal sulfides is controlled by variations of fO_2 and aH_2S. During the earliest stages of serpentinization, the production of H_2 (eq. 1) leads to a strong decrease of fO_2, while the aH_2S of the serpentinizing fluid (i.e., seawater) is expected to be low, hence favouring mantle sulfides dissolution (Klein and Bach, 2009; Schwarzenbach et al., 2012). Sulfur is oxidized and stored as sulfate in serpentine minerals; seawater acting as the major oxidizing agent (Debret et al., 2017). At this stage, sulfur stored in serpentine minerals originates from both mantle and seawater as evidenced by mixed isotopic signatures between seawater and the mantle of sulfate-rich serpentinites (Alt et al., 2013; Alt and Shanks, 1998, 2003; Delacour et al., 2008a). These processes would primarily occur in settings where the serpentinization fluid composition is close to seawater (Alt et al., 2013), such as ultra-slow spreading ridges and deeps at fast spreading ridges.

The precipitation of hydrothermal sulfides results from an increase of aH_2S and/or a decrease of fO_2 (Klein and Bach, 2009; Schwarzenbach

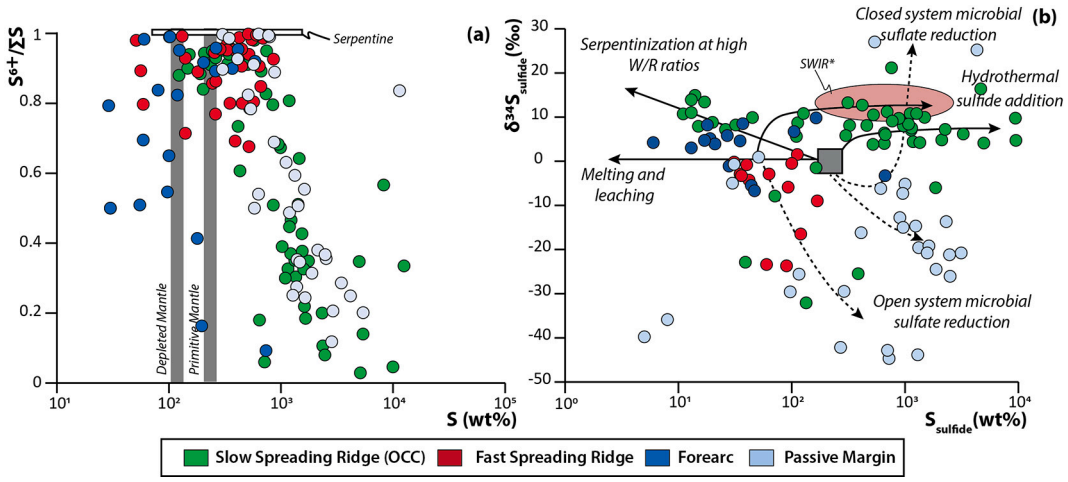

Fig. 3. Geochemical behaviour of sulfur in abyssal serpentinites. (a) $S^{6+}/\sum S$ and (b) $\delta^{34}S$ sulfide plotted against total sulfur and sulfide contents, respectively (dataset used is from Electronic Appendix Table S2). The Fig. 3b shows processes affecting the sulfur isotope composition of sulfide in serpentinites (after Alt et al., 2007; Delacour et al., 2008a; Schwarzenbach et al., 2013). *prediction of ultra-slow spreading ridge serpentinite $\delta^{34}S$ sulfide composition based on Ding et al. (2021).

et al., 2012). This process is particularly active at high-temperature sites near black smokers driven by emplacement of magmatic bodies at depth (e.g., Rainbow hydrothermal site) and is accompanied with a strong increase of [S] and decrease of $S^{6+}/\sum S$ in bulk rock (Fig. 3a). There, seawater percolation into the gabbroic units of the heterogeneous lithosphere is accompanied by sulfide leaching, producing H_2S-rich fluids (Alt and Shanks, 2003; Charlou et al., 2002). The percolation of these fluids in abyssal serpentinites promotes sulfate reduction and hydrothermal sulfide precipitation. These processes are well documented at slow-spreading ridges. Today, no sulfur isotope studies of ultra-slow spreading serpentinites are available for comparison. However, recent analyses of sulfides associated with hydrothermal fields along the South West Indian Ridge show that they can display heavy $\delta^{64}S_{sulfide}$ (9–14 ‰) close to that of slow-spreading ridges (Fig. 3b; Ding et al., 2021).

4.3. Inorganic and organic carbon

The current carbon dataset in abyssal serpentinite worldwide is limited to very few areas, that do not include transform faults (Fig. 4, Table S3). Available data show that the Total carbon concentrations (TC) of abyssal peridotites/serpentinites are highly variable (from 60 ppm to 30 wt%) and overall higher than those of mantle peridotites (50–120 ppm). This attests for a significant storage of carbon during the serpentinization process. In abyssal serpentinites, carbon can be stored as carbonate minerals (TIC: Total Inorganic Carbon) or as carbonaceous materials (TOC: Total Organic Carbon). This is well illustrated by carbon stable isotope values ($\delta^{13}C$; Fig. 4) that spread from an inorganic endmember derived from seawater ($\delta^{13}C_{TIC}$ ~ + 0 to +3 ‰) to an organic endmember ($\delta^{13}C_{TOC}$ ~ - 25 ‰).

On average, the $[C_{TIC}]$ / $[C_{TC}]$ ratio of abyssal serpentinites is about 63 ± 5 % (n = 169), with a mean $[C_{TIC}]$ of 11,351 ± 4992 ppm and a mean $[C_{TOC}]$ of 509 ± 117 ppm. Hence, inorganic carbon is commonly considered as the main carrier of carbon in abyssal serpentinites (e.g., Kelemen and Manning, 2015; Plank and Manning, 2019). In details, the amount of TIC is the highest in passive margin serpentinites ($[C_{TIC}]$ / $[C_{TC}]$ = 67 ± 9 %; $[C_{TIC}]$ = 21,199 ± 10,369 ppm; $[C_{TOC}]$ = 956 ± 299 ppm), where ophicarbonates are abundant, and then in slow spreading serpentinites ($[C_{TIC}]$ / $[C_{TC}]$ = 72 ± 7; $[C_{TIC}]$ = 3994 ± 1862 ppm; $[C_{TOC}]$ = 284 ± 38 ppm), compared to ultra-slow ($[C_{TIC}]$ / $[C_{TC}]$ = 46 ± 12; $[C_{TIC}]$ = n/a; $[C_{TOC}]$ = 220 ± 35 ppm) or forearc ($[C_{TIC}]$ / $[C_{TC}]$ = 45 ± 12; $[C_{TIC}]$ = 503 ± 298 ppm; $[C_{TOC}]$ = 368 ± 49 ppm) serpentinites that display comparable amounts of TIC and TOC. TIC usually corresponds to dolomite or calcite (more rarely magnesite) crystallization from a seawater-dominated fluid at relatively low temperature (< 180 °C) (Lafay et al., 2017; Noël et al., 2018; Schwarzenbach et al., 2013), or from a mixed hydrothermal-seawater fluid at higher T (>200 °C) (Eickmann et al., 2009). Lower temperatures of carbonatation usually

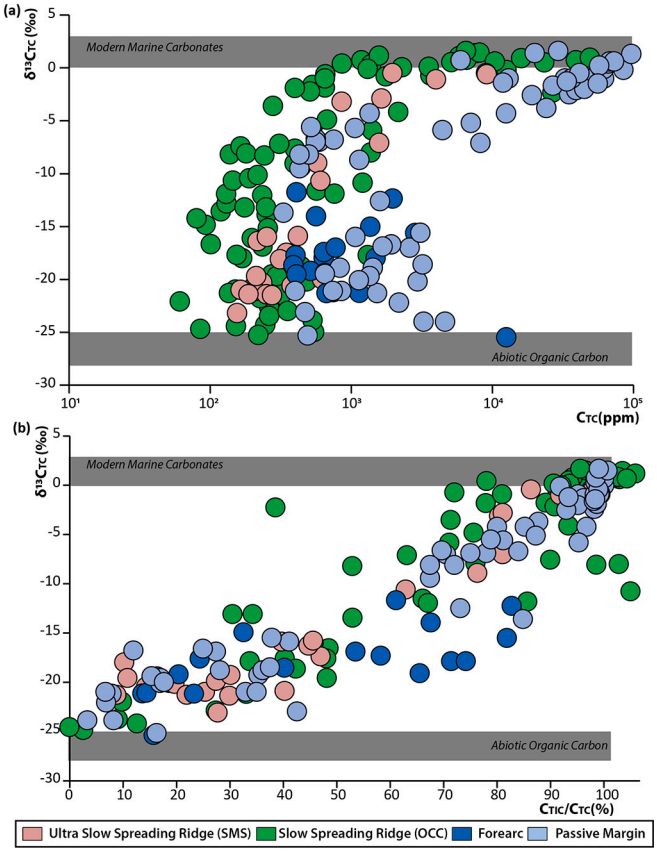

Fig. 4. Carbon isotopes, concentrations (a) and redox state (b) in abyssal serpentinites (dataset used is from Electronic Appendix Table S3). Abiotic organic carbon value is from Debret et al. (2022) and corresponds to the average value of antigorite-bearing serpentinites. Biogenic organic carbon values are widespread, ranging from −30 to −60 ‰ (Früh-Green et al., 2004). The modern marine carbonate value spreads from seawater (0 ‰) to marine carbonates (+3 ‰, Delacour et al., 2008b). (For interpretation of the references to colour in this figure legend, the reader is referred to the web version of this article.)

correspond to authigenic carbonatation (Lafay et al., 2017; Schwarzenbach et al., 2013).

Abyssal serpentinites can have significant amounts of organic carbon, sometimes exceeding those of inorganic carbon whatever the geological setting or tectonic context (Fig. 4b). Observations on ODP Leg 149 and 173 from the Iberian margin show that organic carbon becomes dominant with increasing depth, being the principal carbon phase at more than 50–100 m depth (Schwarzenbach et al., 2013). Similar observations were made in forearc settings, where authigenic carbonates are abundant nearby the summit and flanks of mud-volcanoes, while organic carbon is dominant in the deep lithosphere, below mud-volcanoes (Debret et al., 2022). Organic carbon corresponds to condensed carbonaceous matter of both biological and abiotic origin. It can be made of aromatic and/or aliphatic chains combining C, H and/or N, and are intimately associated with serpentine textures at micro- to nano-scale (Andreani et al., 2023; Debret et al., 2022; Ménez et al., 2018, 2012; Pasini et al., 2013; Sforna et al., 2018). The characteristics of these different types of carbon are the topic of current scientific researches (see review of Andreani and Ménez, 2020 for more details). Today, there is still no established consensus that discriminate the isotope signature of biological versus abiotic organic carbon in abyssal serpentinites.

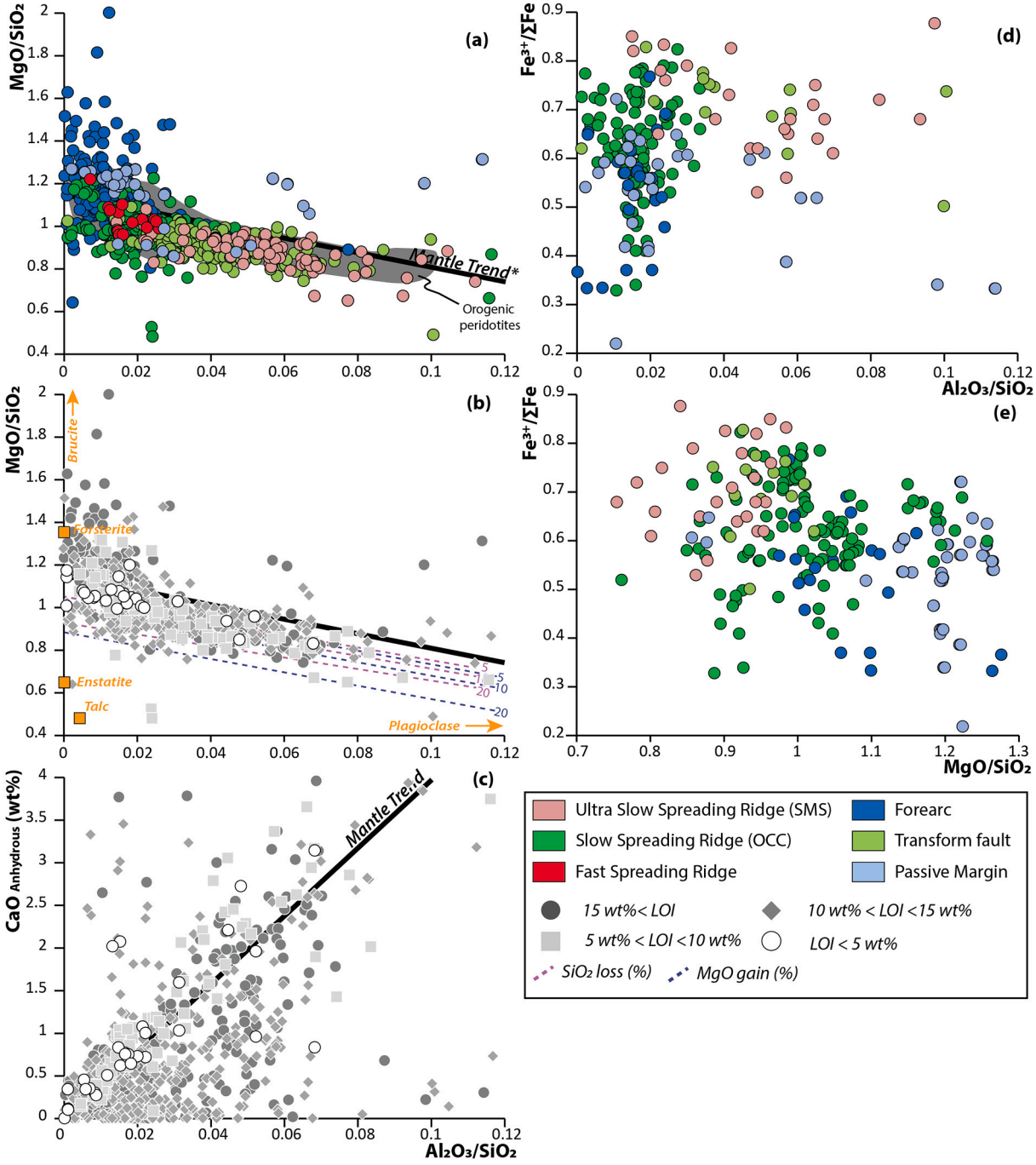

Fig. 5. Major element distribution in abyssal serpentinites. Al_2O_3/SiO_2 ratio against MgO/SiO2 (a-b), CaO (wt%) (c), $Fe^{3+}/\sum Fe$ (d), and MgO/SiO_2 against $Fe^{3+}/\sum Fe$ (e) in abyssal serpentinites (dataset used are from Electronic Appendix Table S1 and S4). The Figure (e) considers samples with L.O.I. values superior to 10 wt%. Mantle trend values and orogenic peridotite field are from Godard et al. (2008) in Fig. 5a-b. The Mantle trend is determined graphically in Fig. 5c. * The mantle trend line is theoric and does not fit orogenic peridotite values (see section 5.1).

Owing to sampling limitation, less is known about carbon distribution and sequestration in the deepest part of the oceanic lithosphere. There is a potential for abiotic organic carbon to be the main carbon carrier in the deepest part of the oceanic lithosphere (>100–200 m) in which inorganic carbon concentration is likely to decrease (Schwarzenbach et al., 2013). This challenges current carbon flux models (e.g., Dasgupta and Hirschmann, 2010; Kelemen and Manning, 2015; Plank and Manning, 2019) that classically consider the sequestration of carbon at MOR by carbonates only (i.e., shallow surface processes).

5. Major, rare earth and trace elements systematics

5.1. Major elements

Whether (or not) serpentinization has consequences on the major element chemistry of peridotites remains an open question (see reviews of Malvoisin, 2015; Mével, 2003; O'Hanley, 1996 to follow this discussion over the last decades). The essence of this problem relates to the changes of both density and volume accompanying peridotite serpentinization. If we consider an exchange of water during serpentinization, the rock density decreases from 3300 kg/m^3 (olivine) to 2900 kg/m^3 (serpentine) while the solid volume can increase by up to 50 % if the system is closed (Coleman and Keith, 1971). In order to compensate for these two effects, the serpentinization process must be isochemical. Indeed, the oxide/SiO_2 ratios between weakly and strongly serpentinized rocks (Fig. 5a-b) overlap and seem to spread between a refractory endmember, poor in Al_2O_3 and rich in MgO corresponding to a dunitic protolith, and a fertile endmember, rich in Al_2O_3 and poor in MgO corresponding to a lherzolitic protolith. However, several authors (Boschi et al., 2008; Komor et al., 1985; Malvoisin, 2015; Niu, 2004; Paulick et al., 2006; Snow and Dick, 1995) noted that abyssal serpentinites exhibit MgO/SiO_2 ratios on average 5 % lower than the mantle (represented by the "mantle trend" line in Fig. 5a-b, calculated using the estimated compositions of the bulk silicate earth or Primitive Mantle by Jagoutz et al., 1979; McDonough and Sun, 1995). This anomaly is often interpreted as a gain in SiO_2 and/or a loss in MgO during the serpentinization process (Malvoisin, 2015; Paulick et al., 2006; Snow and Dick, 1995). However, orogenic peridotite, which are less affected by the serpentinization process (see section 4.1), are also shifted relative to the mantle trend line and overlap with abyssal serpentinite composition. It therefore suggests that the mantle trend line defined by bulk silicate earth or primitive mantle composition poorly fits the measurements of natural mantle peridotites. Hence, the MgO/SiO_2 ratio is a poor proxy for the serpentinization process and associated SiO_2 gain or MgO loss.

There are also abyssal serpentinites with abnormally low MgO/SiO_2 ratios (~0.5; Fig. 5a-b). These compositions could mark a large amount of talc crystallization during serpentinization as these samples display MgO/SiO_2 close to that of talc on Fig. 5a-b. This mineral can form through the percolation of Si-rich fluids for examples near detachment faults (Boschi et al., 2006), or after orthopyroxene during the first stages of peridotite hydration at a high temperature (>350 °C) (Martin and Fyfe, 1970) but is then poorly preserved following olivine serpentinization. Talc is also observed in transform faults recording high temperature alteration (> 500 °C; Prigent et al., 2020). These low MgO/SiO_2 abyssal serpentinites could therefore be specific of (near-)deformation areas.

High LOI serpentinized rocks (LOI > 15 wt%) systematically show high MgO/SiO_2 ratios compared to other serpentinized peridotites (Fig. 5b). This is explained by the presence of brucite (and/or iowaite) in these rocks. The crystallization of this mineral is constrained by high MgO contents reflecting either a refractory protolith or an important mobility of SiO_2 and/or MgO during serpentinization. Yet, although silica can be mobile during serpentinization, many authors agreed that SiO_2 transfers poorly affect Al_2O_3/SiO_2 ratios and that the latter is a good marker of protolith fertility (Deschamps et al., 2013; Malvoisin, 2015; Paulick et al., 2006; Fig. 5b). This is well illustrated in the Al_2O_3/SiO_2 vs. MgO/SiO_2 space where Al_2O_3/SiO_2 variations in abyssal serpentinites are comparable to those of the mantle. Based on Al_2O_3/SiO_2 ratios, most abyssal peridotites have a relatively refractory protolith ($Al_2O_3/SiO_2 < 0.04$). The most refractory protoliths are found in forearc areas (e.g. Mariana) where partial melting rates are expected to be the highest (Parkinson and Pearce, 1998). The most fertile protoliths correspond to rocks analysed at ultra-slow spreading ridges where oceanic expansion is dominantly accommodated by tectonic activity (see section 2.1). Both slow- and fast- spreading serpentinites, display intermediate compositions. In these tectonic contexts, the significant contribution of magmatism to the oceanic extension attests of multiple steps of partial melting and melt/rock interactions impacting the fertility of the protolith and therefore the Al_2O_3/SiO_2 ratios. Few samples from passive margin can display high Al_2O_3/SiO_2 for a given MgO/SiO_2 ratio. These can be attributed to impregnation processes by asthenosphere melt and associated plagioclase crystallization that are commonly reported in this type of setting (e.g., Piccardo et al., 2007). It is important to note that many authors report analyses of "serpentinites" sensu *largo* with anomalous Al_2O_3/SiO_2 ratios (> 0.12). These rocks have a non-peridotitic protolith and are therefore not comparable to abyssal serpentinites sensu stricto. This is particularly obvious for Archean serpentinites that form after ultramafic lavas with high Al_2O_3/SiO_2 and low MgO/SiO_2 ratios (Szilas et al., 2015) or serpentinites formed from pyroxenites or rocks altered at very low temperatures (<<100 °C) that commonly display abnormally high aluminium contents ($Al_2O_3/SiO_2 >> 0.12$; Bodinier and Godard, 2013). These rocks are generally composed of minerals that are not common in abyssal serpentinites (e.g. abnormal abundance of chlorite or amphibole, presence of micas or clays). The geochemical behaviour of these rocks during serpentinization cannot be approached in the same way and these samples were not included in our database.

The mobility of major elements is particularly visible when looking at the CaO contents in abyssal serpentinites. The latter are abnormally low for a given Al_2O_3/SiO_2 ratio compared to mantle peridotites (Fig. 5c). This shows a significant leaching of Ca during the serpentinization process which can be explained by the inability of the serpentine minerals to incorporate Ca cations into their structure. It is interesting to note that few analyses show abnormally high CaO contents relative to that of mantle peridotites ("mantle trend" in Fig. 5c). These analyses attest of a slight Ca enrichment by early fluid- and/or melt- rock interaction processes. For example, the impregnation of the peridotite protolith (e.g., passive margin serpentinites, Fig. 5a) is characterized by the precipitation of plagioclase, increasing both Al and Ca contents in bulk rock. These compositions will favour in turn the precipitation of Ca-bearing phases, such as calcite and amphibole, during hydrothermal alteration. Such phases remain stable during the serpentinization of peridotite, hampering Ca leaching.

When comparing the MgO/SiO_2 and $Fe^{3+}/\Sigma Fe$ ratios in highly serpentinized peridotites in which the $Fe^{3+}/\Sigma Fe$ ratio is not a function of rock hydration anymore (LOI > 10 wt%, see section 4.1), an inverse tendency is observed between these two parameters (Fig. 5e). This suggests that high MgO contents are related to limited Fe oxidation and, therefore, to lower H_2 production during serpentinization. Such a high Mg activity favours early brucite precipitation that incorporates Fe^{2+}, hence limiting the formation of Fe^{3+}-rich serpentine and/or magnetite (e.g., Frost and Beard, 2007), in agreement with previous discussion at end of section 4.1 (Fig. 2). This corresponds to the same two particular geodynamical settings: the forearc area of the Mariana subduction zone and the Iberian abyssal plain. In the case of the Mariana, the protolith is a highly refractory (Mg-rich) peridotite due to extensive flux-melting episodes in the pre-arc position (Parkinson and Pearce, 1998).

At the opposite, serpentinites with the highest $Fe^{3+}/\Sigma Fe$ and the lowest MgO/SiO_2 ratios correspond to serpentinites from the SWIR, where melting rates are expected to be low and peridotite more fertile (Mg-poor, Figs. 5a and e). These observations agree well with

experimental studies showing an important role of protolith modal composition on Fe oxidation kinetics (McCollom and Bach, 2009). The presence of pyroxene inhibits brucite formation during serpentinization as its dissolution increases SiO_2 activity, which favours magnetite and Fe^{3+}-serpentine (Frost and Beard, 2007; Klein et al., 2013). Overall, the geodynamical setting and tectonic context, as related to peridotite fertility, seems to be the main factor controlling Fe oxidation and therefore H_2 productivity at mid-oceanic ridges, with ultra-slow spreading ridges having the highest H_2 productivity.

However, when comparing the Al_2O_3/SiO_2, considered as robust to serpentinization and as a good proxy for protolith fertility, with $Fe^{3+}/\Sigma Fe$ ratios in serpentinites (Fig. 5d), the relationship between protolith fertility and $Fe^{3+}/\Sigma Fe$ ratios in serpentinites disappears. This shows that protolith composition alone cannot be the only factor controlling Fe oxidation and H_2 productivity and that other parameters or processes, related to the geological setting, occur. For example, a low temperature of serpentinization (<250 °C) thermodynamically favours brucite formation relative to magnetite (Klein et al., 2014). This fits well with the temperature conditions (< 200 °C) recorded by serpentinites from Iberian margin (Schwarzenbach et al., 2013) and MgO-rich Mariana (blue-serpentinites; Debret et al., 2019) samples displaying the lowest $Fe^{3+}/\Sigma Fe$ (see sections 2.2 and 2.3). In all the other settings, a higher temperature of serpentinization close to 300 °C was estimated (Table 1).

5.2. Rare Earth elements

Abyssal serpentinites show variable chondrite and primitive mantle normalized rare earth (REE: Rare Earth Elements) and trace elements profiles depending on the geodynamic setting and tectonic context (Fig. 6). A large part of these profiles is inherited from the peridotite protoliths (Andreani et al., 2014; Debret et al., 2013a; Dessimoulie et al., 2020; Niu, 1997, 2004; Paulick et al., 2006). Mantle peridotite REE profiles are controlled by the abundance of pyroxene (see Bodinier and Godard, 2013 for a comprehensive review): lherzolites are characterized by a depletion in light REE (LREE: La to Nd) and flat heavy REE segments (HREE: Tb to Lu), while pyroxene-poor harzburgites or dunites have lower HREE concentrations and their REE profiles are characterized by a progressive depletion from HREE to LREE, with generally flat LREE segments.

The inheritance of peridotite protolith composition is well illustrated when HREE concentrations are plotted against High Field Strength Elements (HFSE) or other fluid immobile elements, such as Th (Fig. 7a), which indicates that magmatic processes (melting, melt-rock interaction) is the dominant factor controlling the compositional variation of abyssal serpentinites (Niu, 2004; Paulick et al., 2006). HREE depletion is most pronounced in forearc serpentinites: their protoliths are thought to be highly refractory sub-arc peridotites formed by extensive flux melting before being carried into forearc position by mantle convection (Parkinson and Pearce, 1998). However, large deviations relative to melt/rock trends can be observed (Fig. 7b-c), by comparing LREE (or Middle REE – Sm to Gd) to HREE at relatively constant Th concentrations (about 3 to 4 order of magnitude). Paulick et al. (2006) interpret these variations as an evidence for L-MREE mobility in hydrothermal fluids during serpentinization process.

5.3. Cerium and europium anomalies

The influence of the serpentinization conditions is more pronounced when looking at Ce and Eu anomalies (Fig. 6) that imprint different signatures on the REE patterns among the geodynamical settings and tectonic contexts. Both Ce and Eu anomalies do not covary with tracers of melt/rock interactions such as HFSE or Th (Fig. S2). The fractionation of these elements is typically interpreted as indicators of redox variations with the formation of Ce(IV) in oxidative environments and Eu(II) in reducing environments. This change of valence induces a change of chemical behaviour with respect to the neighbouring valence (III) elements and beyond the differences in ionic radius that characterizes REE.

The mobility of Ce depends on its redox state and fluid pH. It is generally accepted that Ce is immobile in oxidized form under neutral pH (e.g., seawater) but that it becomes mobile, in a similar way to neighbouring LREE, at low pH and in reducing conditions (Allen and Seyfried Jr, 2005). In abyssal serpentinites, the negative Ce anomaly is interpreted as the percolation of oxidizing seawater (Dessimoulie et al., 2020; Frisby et al., 2016; Rouméjon et al., 2014). Frisby et al. (2016) support this interpretation in the SWIR serpentinites by reporting high U/Th ratios associated with negative Ce anomaly (Fig. 8). Both U and Th are incompatible elements and Th is considered as immobile in fluids. The authors attribute the increase of U/Th ratio to an addition of U by the serpentinizing fluid in oxidizing conditions (U(VI)) and the negative Ce anomaly by the addition of La(III) and Pr (III), assumed to be fluid-mobile relative to Ce(IV) under these conditions. Fig. 8 shows that this anomaly is characteristic of ultra-slow spreading ridges and transform faults serpentinites. It is worth noting that these negative Ce anomalies are not related to a late overprint by seawater, e.g., related to a longer resident time of the samples on the seafloor as expected at passive margins or for dredged samples relative to drilled ones. Indeed, although Ce anomalies are reported in samples collected by dredges or dives at ultra-slow spreading ridges or transform faults (Fig. 6), few to no Ce anomalies were reported at passive margins or slow-spreading contexts where samples were collected by both dill and dredge methods (Figs. S1 & S3). At transform faults, abyssal serpentinites can also display positive Ce anomalies with very low U/Th ratios and enrichments in LREE (Fig. 6e). These serpentinites had to form after a protolith abnormally enriched in LREE prior to a serpentinization stage by seawater that leached all LREE but Ce, immobile in seawater. These two types of Ce anomalies and LREE patterns suggest that serpentinites observed at transform faults formed after peridotites with highly variable LREE/M-HREE ratios, and that the mantle sampled in this context is more heterogeneous relative to other contexts. In addition, this characteristic REE pattern of transform fault serpentinites (Fig. 6e-f) is very distinct to the ones of fast- and slow-spreading serpentinites (Fig. 6b-c; e.g., Eu anomaly). This suggests that serpentinites collected so far at transform

Table 1
Main characteristics of abyssal serpentinites according to geological settings and tectonic contexts. * Maximum depth of serpentinization, see section 2 for more details.

Geodynamical Setting	Tectonic setting	Maximum Depth*	Temperature	Main Mineralogy	Sampling Methods	Sampling Areas
Mid-Ocean Ridges	*Slow Spreading Ridges*	4 km	300–500 °C	Liz/Ctl-Mag	Drilling-Dredging-Insitu sampling	North Atlantic Ridge
	Ultra-Slow Spreading Ridges	5 km	200–300 °C	Liz/Ctl-Mag	Dredging-Insitu sampling	Gakkel Ridge, South West Indian Ridge
	Fast Spreading Ridges	?	200–350 °C	Liz/Ctl-Mag	Drilling	East Pacific Rise
	Oceanic Transform Faults	9 km	120–550(?)° C	Liz/Ctl-Mag	Dredging-Insitu sampling	North & Central Atlantic Ocean, Central & South West Indian Ocean, American-Antarctic Ocean, Pacific-Antarctic Ocean
Forearc		15 km	180–420 °C	Liz/Ctl-Brc or Atg-Brc-Mag	Drilling-Dredging-Insitu sampling	Mariana, Guatemala, Tonga, South Sandwish, Trench fracture zone intersection
Passive Margin		5 km	< 200 °C	Liz/Ctl-Bru	Drilling	Iberian abyssal plain, Newfoundland

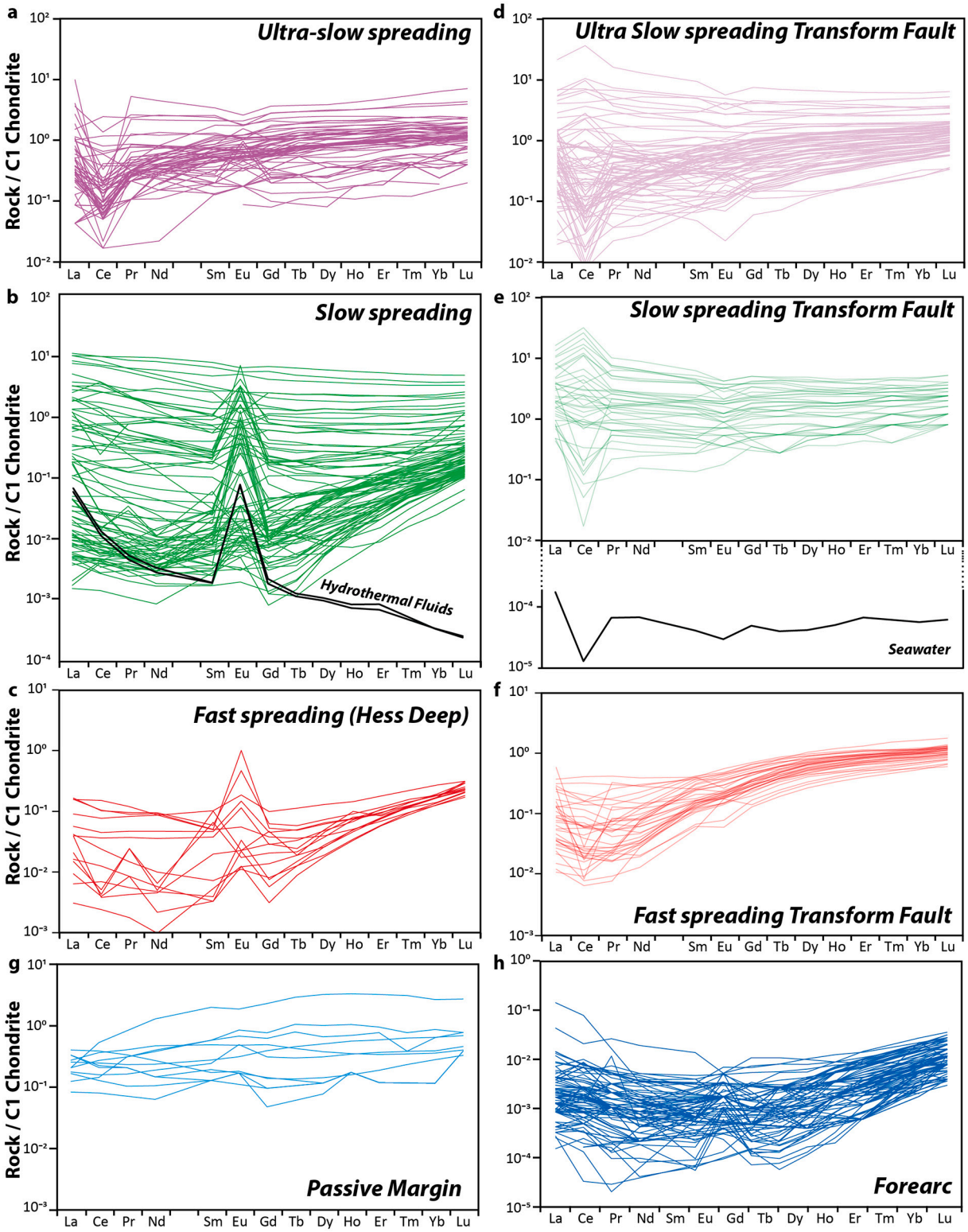

Fig. 6. Representative REE profiles of abyssal serpentinites as a function of geodynamical setting (dataset used is from Electronic Appendix Table S4). Samples are compared according to localities: samples from (a) the SWIR (Ultra-slow spreading) are compared to (d) transform faults crossing the SWIR (for sake of clarity only samples from the Marie Celeste, Atlantis II, Bouvet, Islas Oscadas, Prince Edward, Shaka, Vulcan and NW Bullard were plotted), (b) the 15°20' Fracture Zone (Slow spreading) are compared to (e) Vema transform fault, (c) Hess Deep (Fast spreading) are compared to (f) the Udinstev transform fault. Only Mariana forearc REE profiles are displayed in (h). A full overview of worldwide REE profiles is provided in Fig. S1. Seawater and hydrothermal fluid values are from Douville et al. (2002).

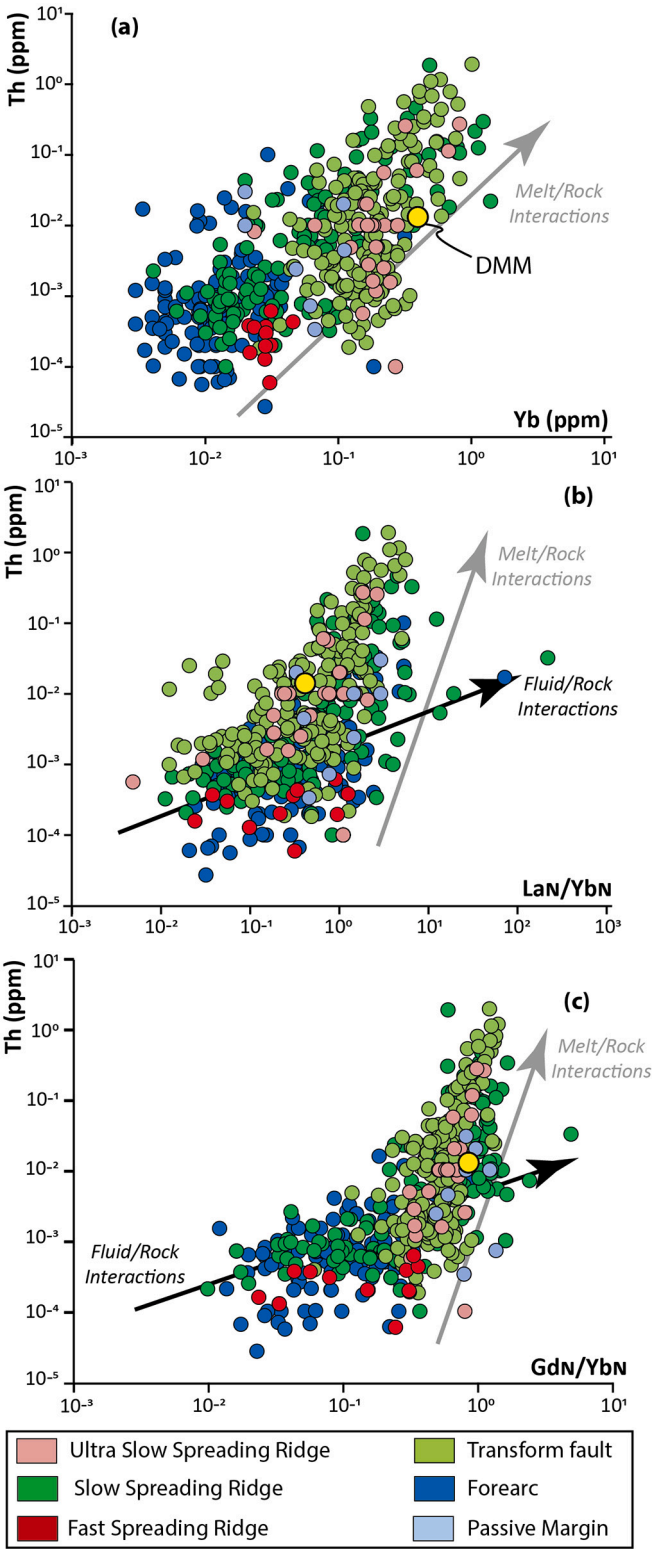

Fig. 7. Melt/rock versus Fluid/rock influence in abyssal serpentinite geochemistry. Th versus (a) Yb concentrations in ppm, (b) La_N/Yb_N and (c) Gd_N/Yb_N in abyssal serpentinites (dataset used is from Electronic Appendix Table S4). The Melt/Rock and Fluid/Rock interaction trends are from Paulick et al. (2006). N: chondrite normalized. DMM: Salters and Stracke (2004).

faults, whatever the type of spreading rate, were not affected by axis processes and are therefore formed in situ by later interaction between seawater and fresh peridotites.

Europium has different charges and ionic radii depending on temperature and redox conditions, with Eu^{2+} being mobile in fluids and Eu^{3+} being relatively immobile (Allen and Seyfried Jr, 2005). This affects the ratio of Eu concentrations relative to the neighbouring REE (Sm and Gd) in serpentinites (Fig. 6). The Eu anomaly is dominant feature of REE patterns of slow-spreading serpentinites suggesting that Eu has been mobilized under divalent state in high T fluids before being stored in serpentinites in trivalent form under lower T conditions. This observation fits well with the reducing nature and high T of hydrothermal fluids observed in this tectonic context at HT black smokers (see sections 2 and 4.2, and Fig. 6b; Charlou et al., 2002). There, the significant magmatic activity provides heat and Eu source which modifies the fluid (e.g., Alt and Shanks, 2003) prior to serpentinization at shallower levels, more propitious for Eu oxidation and storage in rocks. Since the ionic ratio of Eu is theoretically too large to be structurally substituted in serpentine minerals, the Eu anomaly may be accommodated by other processes (i.e., mineral surface processes) or phases. Indeed, Eu positive anomaly is a common feature of massive sulfides associated with HT hydrothermalism (Zeng et al., 2015). The precipitation of hydrothermal sulfides could contribute to the appearance of Eu anomalies in abyssal serpentinites (e.g. Rainbow, Andreani et al., 2014). The absence of the Eu anomaly in other settings suggests either the absence of an Eu source or an aqueous geochemistry of Eu dominated by the trivalent state and low temperature processes. As the serpentinization T is similar in all tectonic contexts (see section 2), the absence of an Eu source, such as magmatic units, during the course of fluid is favoured.

Overall, the predominance of either Ce or Eu anomalies is less evident in geodynamical settings or tectonic contexts (Fig. 6) other than (ultra-)slow-spreading ridges and transform faults. This is well illustrated on Fig. 8b where ultra-slow spreading ridges and transform faults serpentinites plot along the Eu* axis of the primitive mantle, while they display highly variable Ce* (from negative to positive anomalies). At the opposite, slow-spreading ridges serpentinites plot along primitive mantle Ce* axis and display highly variable Eu* showing a high mobility of both Eu and Ce in fluids. This dichotomy between abyssal serpentinites formed at ultra-slow spreading ridges and transform faults, versus slow-spreading ridges, is similar to that report for sulfur (see section 4.2). It shows that fluid/rock interaction between magmatic rocks and serpentinites deeply impact the redox state (i.e., fO_2) of the serpentinizing fluids, favouring the mobility of redox sensitive elements, such as Eu, Ce and S, at depth.

5.4. Fluid mobile elements

Among trace elements, the fluid mobile ones (FME: U, B, Li, As, Sb, Pb, Sr, Rb and Cs) are particularly affected by the serpentinization process as testified by frequent positive (or more rarely negative) anomalies of these elements on abyssal serpentinite spidergrams (e.g., Deschamps et al., 2013; Peters et al., 2017; see also Fig. S4).

Uranium has the particularity of being both incompatible and highly mobile in fluids. Abnormally high U concentrations in abyssal serpentinites can therefore be attributed to either magmatic and/or hydrothermal processes. In order to decorrelate these effects, uranium is often normalized to thorium, which has similar physico-chemical properties to uranium, being also incompatible, but immobile in fluids. Hence, by comparing U/Th ratios of serpentinites with that of the primitive mantle, we see that this element is strongly enriched in serpentinites (Fig. 8), showing a storage of U over Th during serpentinization.

Concentrations of alkali and alkaline metal, such as strontium, rubidium and caesium, in abyssal serpentinites are influenced by both melt/rock interactions affecting peridotites prior to serpentinization, leading for example to Sr- and alkali-rich plagioclase crystallization (e.g., impregnation processes; Drouin et al., 2009), and/or by the

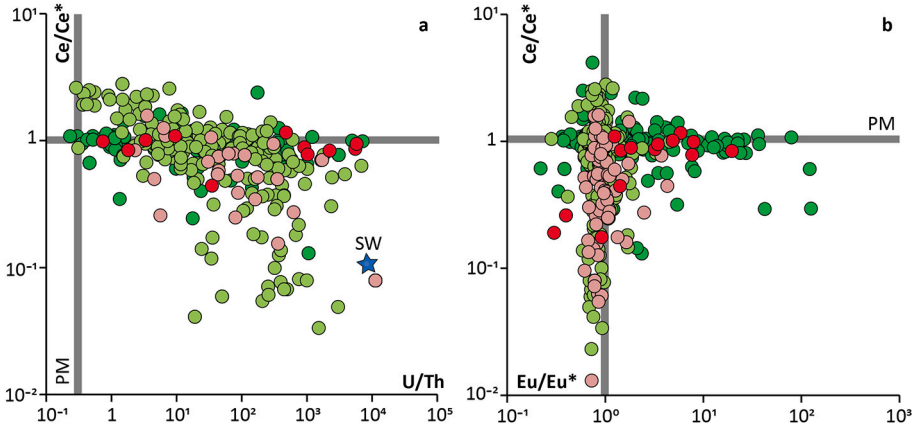

Fig. 8. Ce and Eu anomalies in abyssal serpentinites. (a) U/Th vs Ce/Ce* and (b) Eu/Eu* vs Ce/Ce* ratios in abyssal serpentinites from transform faults, ultra-slow and slow spreading ridges (dataset used is from Electronic Appendix Table S4). Seawater values are from Turekian (1968). Primitive mantle values are from McDonough and Sun, 1995. The symbol colour is the same as Fig. 7.

serpentinizing fluid composition. Carbonatation is also expected to increase alkali concentrations, with ophicarbonates displaying high Cs, Rb, and Sr relative to serpentinites (Schwarzenbach et al., 2021). However, such a process also increases Ca concentrations. Our data filtering (see section 3) should therefore avoid the influence of carbonatation in the data compilation. Most of abyssal serpentinites display a correlation between U/Th ratios and Sr, Rb or Cs, showing that these elements are added during the serpentinization process. Only forearc serpentinites show preferential addition of Sr and Cs over U and Rb (Fig. 9a-b). This highlights the role of slab derived fluids which are likely to be derived from Sr and alkali-rich sediments and depleted in U or Rb (Peters et al., 2017).

Among FME, B has received particular attention in recent years since abyssal serpentinites constitute the main reservoir of B in the oceanic lithosphere (Marschall, 2018). Boron is particularly enriched in seawater relative to mantle peridotites and highly sensitive to pH, such that at pH > 8.6, borate ion dominates in aqueous solution while at lower pH boric acid is the dominant species (Hershey et al., 1986). There is a large overlap of abyssal serpentinite boron concentrations between the different serpentinization settings, with most of abyssal serpentinites displaying boron concentration between 10 and 100 ppm and an average value of 38 ppm (Fig. 9c). Serpentinites from the forearc (B_{mean} = 25 ppm), slow (B_{mean} = 35 ppm) and fast spreading ridge (B_{mean} = 27 ppm) are less enriched in B compared with serpentinites formed at ultra-slow (B_{mean} = 58 ppm) spreading ridges, transform fault (B_{mean} = 58 ppm) and passive margin (B_{mean} = 99 ppm).

Abyssal serpentinites have highly variable Li contents, with some samples depleted in Li relative to the primitive mantle (Fig. 9c). Serpentine minerals incorporate low Li contents (generally less than 1 ppm) compared with mantle minerals (0.1–10 ppm; Vils et al., 2008) suggesting that the observed variability is inherited from peridotite protolith while Li is mainly leached in fluids during serpentinization. It is generally accepted that the Li budget of the oceanic lithosphere is carried by other rocks (e.g. altered mafic crust) and that serpentinites play a lesser role in lithium geochemical cycle.

Arsenic and antimony are two redox sensitive metalloids, usually considered as having a similar behaviour during the serpentinization process (e.g., Deschamps et al., 2011). Antimony solubility is controlled by the formation of secondary minerals that can store Sb as Sb(III) (e.g., spinels such as Sb_2O_3), while serpentine minerals incorporate lower concentrations of Sb(V). As such, a reduction of Sb(V) into Sb(III) favours a decrease of Sb solubility and the storage of this element. Arsenic is stored under As(V) in serpentine (Hattori et al., 2005) or spinel. The partition coefficient of this element remains constant throughout the serpentinization reaction whatever the variations in redox condition or fluid composition (Lafay et al., 2016). As and Sb concentrations of serpentinites overlap worldwide (Fig. 9d). Only forearc serpentinites tend to display low As and Sb concentrations relative to serpentinites derived from other geodynamical settings, once highlighting the particularity of serpentinizing fluids derived from the slab.

It is worth noting that some decoupling behaviour between As and Sb can be highlighted among the geodynamical settings. Such decoupling was also observed in experimental investigation during olivine serpentinization in hydrothermal alkaline systems (Lafay et al., 2016) and was attributed to variation of Sb redox state.

At ultra-slow spreading ridges, abyssal serpentinites display Sb/As ratios close to that of seawater. The oxidation of Fe during serpentinization should favour a decrease of fO_2 in water and, therefore, a decrease of Sb solubility. This process leads to the storage of both As and Sb in serpentinites.

At slow spreading ridges, the redox states of both Sb and As in the serpentinizing fluid are dominated by reaction between seawater and gabbros occurring prior to serpentinization (see sections 4.2 and 5.3) favouring a reduction of Sb(V) to Sb(III) and therefore limiting Sb mobility in fluids compared to As. This could lead to a decoupled behaviour between As and Sb in this tectonic context (i.e., preferential addition of As and decrease of Sb/As ratios, Fig. 9d-e). In agreement with this, Breuer and Pichler (2013) estimated that hydrothermal fluids at the Mid-Atlantic Ridge should contain up to 24 $\mu g.L^{-1}$ of As, while Sb hydrothermal fluids concentrations vary between 0.37 and 1.34 $\mu g.L^{-1}$ (Douville et al., 2002). This leads to Sb/As ratios inferior to <<0.06, so between 2 and 10 times lower than seawater (Sb/As = 0.13, Li, 1991) in agreement with As and Sb variations in this setting (Fig. 9d).

Intriguingly, transform fault serpentinites display similar As and Sb composition with slow spreading ridge serpentinites, while these rocks are expected to be serpentinized by seawater derived fluids that are not affected by interaction with gabbroic units (see section 5.3, Fig. 9d-e). This could be attributed to low water / rock ratios at depth favouring a redox re-equilibration of the serpentinizing fluid with the host rock (i.e., reduced conditions associated with H_2 production limiting Sb mobility), while at ultra-slow spreading context, the more abundant fluid circulation should favour a redox disequilibrium between the oxidizing serpentinizing fluid (seawater) and the host rock.

In forearc settings, the relatively low Sb/As ratios and Sb concentrations of serpentinites must be attributed to either a protolith highly depleted in Sb, a low solubility of this element in slab derived fluids and/or a leaching of this element during serpentinization which can occur if fluids are sufficiently oxidized during serpentinization (Fig. 9e). Overall, these results highlight different redox conditions during abyssal serpentinization processes leading to a preferential incorporation of As over Sb during the serpentinization.

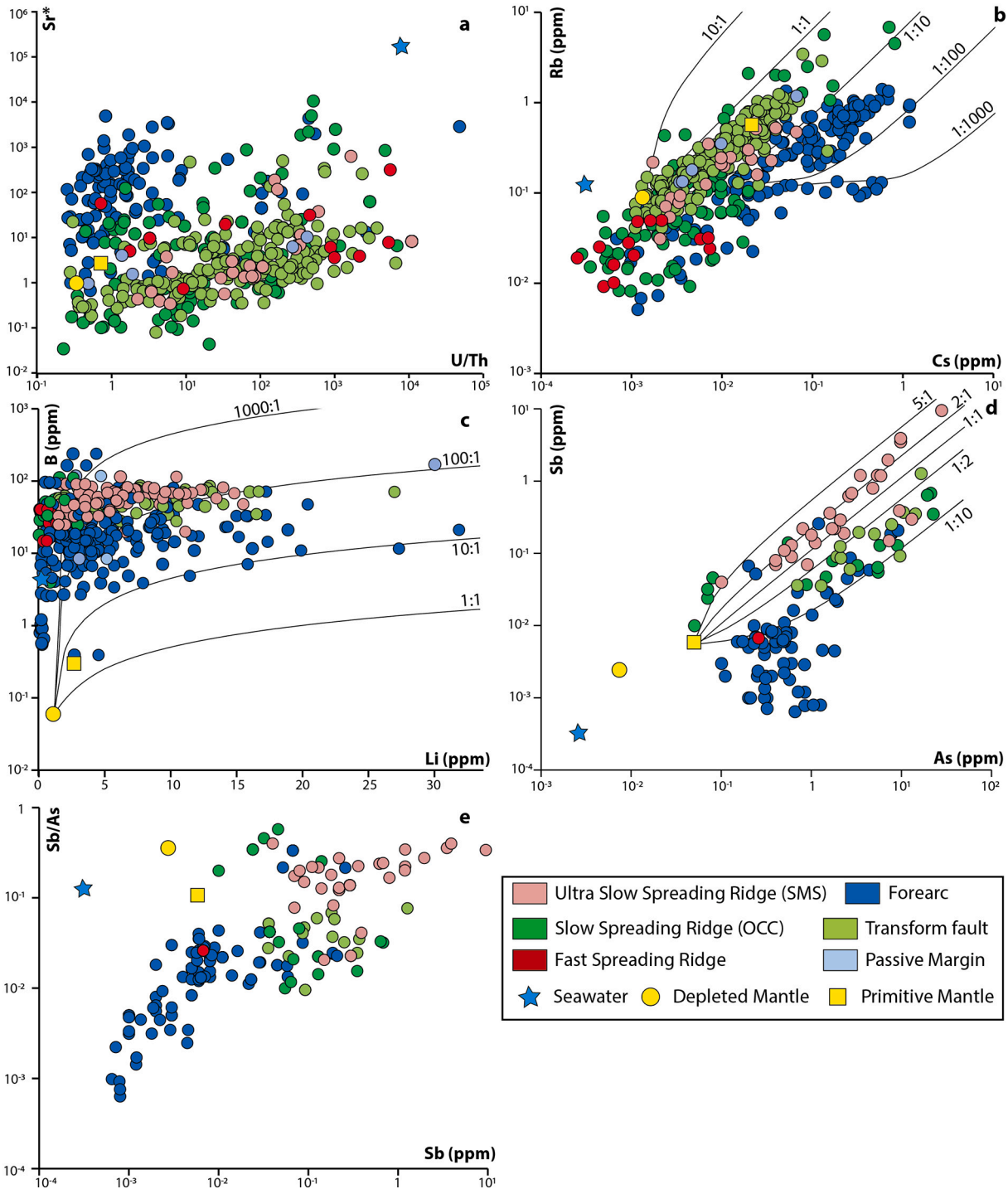

Fig. 9. FME variations in abyssal serpentinites. (a) Sr* (= Sr_n / [(Pr_n + Nd_n)/2], n: primitive mantle normalized) vs U/Th, (b) Rb vs Cs, (c) B vs Li, (d) Sb vs As and (e) Sb/As vs Sb. Primitive mantle values are from McDonough and Sun (1995), depleted mantle values are from Salters and Stracke (2004) and seawater values are from Turekian (1968). Evolution lines for linear enrichments were calculated either using depleted or primitive mantle values (note that variable melt extraction and/or melt/rock interaction are expected to shift the starting point of these models).

6. Transition metals mobility: An isotope approach to constrain fluid geochemistry

Ultramafic host hydrothermal sites are often associated with a significant mobility of metals (e.g., Cu, Zn, Co, Au, and Ni) in fluids (Fouquet et al., 2010). The source of these metals results either from the interaction of seawater with mantle peridotites and/or be an admixture of fluids escaping from mafic bodies at depth. The use of transition metal stable isotopes (e.g., Fe, Zn, and Cu) provides key constraints on the mobility of these elements in fluids and therefore on mass balance of metals exchanges between the lithosphere and oceans. The dataset on Fe-Zn-Cu stable isotopes is currently limited to slow (Rainbow massif, MARK), ultra-slow (Gakkel ridge, SWIR) and transform faults (Shaka, Prince Edward) tectonic contexts and the Mariana forearc setting (Electronic Appendix Table S5).

6.1. Iron isotopes

The first Fe isotope analyses (δ^{56}Fe) in abyssal serpentinites were presented by Craddock et al. (2013). These authors show greater variability of δ^{56}Fe (-0.10 ‰ < δ^{56}Fe < $+0.11$ ‰) in abyssal serpentinites compared with the primitive mantle ($+0.03 \pm 0.01$ ‰; Sossi et al., 2016). However, a large fraction of these analyses has high CaO contents (>4 wt%) and/or Al_2O_3/SiO_2 ratios (>0.12), consistent with the observation of weathering surface (Craddock et al., 2013), suggesting late partial re-equilibration with seawater at very low temperatures (<100 °C). These features are not consistent with serpentinization processes (see sections 3.1 and 5.1). When these anomalous data are discarded, the abyssal serpentinites analysed by Craddock et al. (2013) display δ^{56}Fe values between -0.06 ‰ and + 0.05 ‰, similar to that of mantle peridotites. In Fig. 10a, the absence of correlation between δ^{56}Fe and LOI in abyssal serpentinites suggests a limited impact of the serpentinization on Fe mobility in hydrothermal fluids. Conversely, in Fig. 10b, δ^{56}Fe values vary with Al_2O_3/SiO_2 ratios, spreading between a fertile endmember, enriched in heavy isotope, and a refractory and isotopically light endmember. These observations suggest that Fe isotopes are poorly fractionated during the serpentinization processes and that this process alone cannot explain the high mobility of Fe observed in hydrothermal fluids (Debret et al., 2018). However, when comparing different tectonic contexts with contrasting fertility of the peridotite protoliths, samples from ultra-slow spreading ridges ($+0.01 \pm 0.02$ ‰) show comparable δ^{56}Fe values relative to samples from slow spreading ridges (-0.03 ± 0.05 ‰), overlapping within an error with that of the primitive mantle ($+0.03 \pm 0.01$ ‰; Sossi et al., 2016). This suggests a limited influence of melting processes on the signature of δ^{56}Fe at mid-oceanic ridges.

Peridotite minerals (olivine and pyroxene) display isotopic signatures close to +0.02 ‰ (Sossi et al., 2016). Among serpentinite forming minerals, serpentine has a light isotopic signature (< −0.3 ‰) in contrast to Fe-rich phases, such as magnetite or awaruite that have isotopically heavy signatures (> +0.3 ‰; Scott et al., 2017). This suggests a redistribution of Fe at sample scale between the newly formed minerals. These results agree with theoretical calculations of isotopic fractionation coefficients predicting a preferential incorporation of heavy Fe in Fe^{3+}-oxides (e.g., Polyakov and Mineev, 2000). Hydrothermal sites are typically associated with strong magnetic anomalies (Szitkar et al., 2014) suggesting the precipitation of large amount of magnetic minerals within the hydrothermal plumbing system. Extensive magnetite precipitation could potentially explain the release an isotopically light Fe-rich fluids in ultramafic-hosted hydrothermal systems. This scenario agrees with recent analyses of isotopically heavy mineralized serpentinites containing a large amount of sulfides and magnetite near hydrothermal sites (Debret et al., 2018) and with the occurrence of magnetite rich deposits associated with ultramafic-hosted paleo-hydrothermal systems in ophiolites (Hodel et al., 2017; Toffolo et al., 2017). However, the origin of these formations and the mechanisms enhancing magnetite deposits in these settings remain poorly constrained and they are debated in the literature (Hedenquist and Lowenstern, 1994; Rouxel et al., 2003).

Forearc serpentinites stand out as an isotopically light Fe endmember, with an average value of -0.06 ± 0.03 ‰ and values as low as -0.26 ± 0.06 ‰ (Fig. 10). These light values are difficult to explain with melting models, the later predict that even large (>30 %) degrees of melt extraction do not generate strongly fractionated residues (< 0.1 ‰; Dauphas et al., 2017; Sossi and O'Neill, 2017; Williams et al., 2004; Williams and Bizimis, 2014). These samples correspond to antigorite-bearing serpentinites, recording high temperature of serpentinization (> 320 °C). Negative correlations between serpentinite bulk δ^{56}Fe, fluid-mobile element concentrations (e.g., B, As) and $Fe^{3+}/\Sigma Fe$ suggest that these δ^{56}Fe values could reflect the transfer of isotopically light iron by slab-derived fluids (Debret et al., 2020).

6.2. Zinc and copper isotopes

Zinc (δ^{66}Zn) and copper (δ^{65}Cu) isotope ratios of mantle peridotites are little affected by melting and late magmatic processes and the average value of the primitive mantle is estimated at $+0.16 \pm 0.06$ ‰ and $+ 0.07 \pm 0.10$ ‰, respectively (Moynier et al., 2017; Savage et al., 2015; Sossi et al., 2018). The Zn and Cu budget in mantle peridotites is controlled by Zn rich spinels and Cu rich sulfides, respectively (up to several hundred ppm compared to mantle silicates, about 10–50 ppm; Guo et al., 1999; Hodel et al., 2018; Wang et al., 2017). When comparing Zn and Cu isotope ratios of abyssal serpentinites formed at forearc, transform fault, slow and ultra-slow spreading ridges, two trends are evident (Fig. 10c-d): transform fault and ultra-slow spreading ridges serpentinites show a Zn and Cu depletion and high δ^{66}Zn and δ^{65}Cu isotope ratios relative to that of the primitive mantle, while slow spreading ridges serpentinites display relatively high Zn and Cu concentrations and highly variable isotope ratios.

At transform faults and ultra-slow spreading ridges, the serpentinization is accompanied with a progressive disappearance of mantle minerals, including the oxidation of mantle sulfides to sulfate bearing serpentine (Debret et al., 2017) and oxidation of Fe^{2+}-bearing olivine mainly into Fe^{3+}-bearing serpentine (see section 4.1). Given that serpentine minerals incorporate low Zn and Cu concentrations (<10 ppm; Rouméjon et al., 2014), these abyssal serpentinization contexts should therefore favour an important leaching of Zn and Cu in hydrothermal fluids. Such process can be modelled through a Rayleigh distillation considering the dissolution of sulfides and spinel by chlorine-bearing fluids ($ZnCl_4^{2-}$ or $CuCl_3^-$) during the serpentinization (see Supplementary Material for modelling details). In these models, the elemental and isotopic behaviour of Zn and Cu in whole rock is approximated to that of sulfides, spinels or silicates. We used the ab initio calculations of Fujii et al. (2014) for $ZnCl_4^{2-}$ and $CuCl_3^-$ complex in fluids, those of Ducher et al. (2016) for sphalerite (ZnS), different spinel endmembers, namely franklinite ($ZnFe_2O_4$), gahnite ($ZnAl_2O_4$) and zincite (ZnO), and those of Liu et al. (2021) for villamaninite (CuS_2), chalcopyrite ($CuFeS_2$) and Cu-bearing enstatite ($Mg_{31/16}Cu_{1/16}Si_2O_6$). Results of these models are displayed in Fig. 10e-f. As expected, the dissolution of sulfide has only a limited effect on δ^{66}Zn of abyssal serpentinites (e.g., sphalerite on Fig. 10e) while it can explain most of δ^{65}Cu variations (e.g., chalcopyrite or villamaninite on Fig. 10f). At the opposite, the dissolution of mantle spinels leads to strong Zn isotope fractionation, up to ~1 ‰, and can explain most of the fractionated composition of transform fault and ultra-slow spreading ridges serpentinites. It is interesting to note that the preferential partitioning of Cu in silicates may lead to unexpected high Cu isotope fractionation during the serpentinization process and may explain the high δ^{65}Cu observed in some Cu-poor samples. Sulfide, spinel and silicate dissolutions by seawater like fluids can therefore explain the isotope composition of abyssal serpentinites generated at transform faults and ultra-slow spreading ridges. It is important to note that consideration of sulfur, carbon or aqueous complexes in the fluids will lead to isotope fractionations that are not compatible with abyssal serpentinite composition (Fig. S5). Few samples display abnormally high Zn and Cu concentrations and isotopically light values. These serpentinites are rare and might correspond to serpentinites equilibrated with external fluids (see section below).

Forearc serpentinites tend to display a similar behaviour relative to transform faults and ultra-slow spreading ridges serpentinites for Zn isotopes, although few samples have higher zinc concentrations than primitive mantle (Fig. 10c). In this context, a leaching of Zn is therefore also expected. It suggests a limited transfer of Zn by slab derived fluids. It is worth noting that apparently light Zn values were reported in this geodynamical setting (Pons et al., 2011). However, the absence of specific protocols for dissolving spinel in Pons et al. (2011) and the different values reported here lead us to discard these values.

At slow spreading ridges, abyssal serpentinites display large

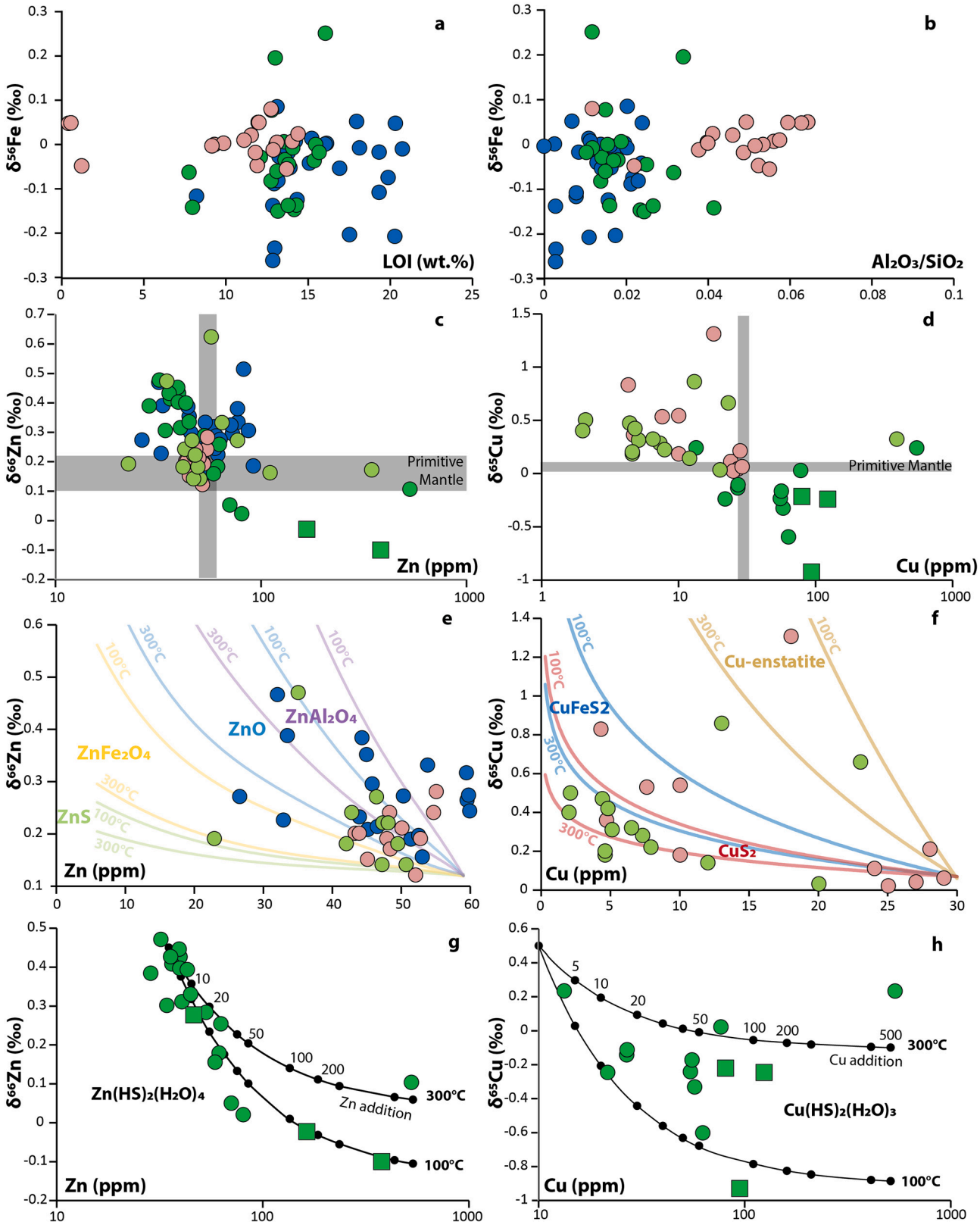

Fig. 10. Metal stable isotope variations in abyssal serpentinites. Fe (a-b), Zn (c,e,g) and Cu (d, f, h) isotope ratio variations versus Loss On Ignition (L.O.I.), Al_2O_3/SiO_2, Zn and Cu concentrations (dataset used is from Electronic Appendix Table S5). Fig. 10e and f display Rayleigh distillation models (coloured lines) between seawater like fluids ($ZnCl_4^{2-}$ and $CuCl_3^-$) and minerals. In these figures, the abyssal serpentinite compositions are modelled by a leaching of $ZnCl_4^{2-}$ and $CuCl_3^-$ anions in fluids during the dissolution of sulfides (ZnS, CuS and $CuFeS_2$), spinels ($ZnFe_2O_4$, ZnO, $ZnAl_2O_4$) and silicate (Cu-enstatite) at temperatures between 100 and 300 °C. Fig. 10g and h display additional mixing model results (black lines) corresponding to an addition of Zn and Cu by HS-rich fluids at temperatures between 100 and 300 °C. Green squares correspond to mineralized samples in Debret et al. (2018). (For interpretation of the references to colour in this figure legend, the reader is referred to the web version of this article.)

variations of Zn and Cu concentrations and isotope ratios (Fig. 10c-d). In this tectonic context, the hydrothermal circulation is influenced by gabbroic intrusion which supply both a heat source and an important metal reservoir, i.e., fresh MORB contain between 50 and 80 ppm of Zn and between 30 and 220 ppm of Cu mainly stored in sulfides. The reaction between seawater and gabbro is therefore expected to produce high temperature (>350 °C), sulfur- (HS_2) and metal- rich fluids (Alt and Shanks, 2003). As they rise to the surface, the oxidation of sulfur-rich hydrothermal fluids in contact with seawater leads to abundant precipitation of sulfides and/or magnetite within the hydrothermal stockwork. This process was further explored by Debret et al. (2018) who investigated mineralized serpentinites, with high amount of sulfides, formed near active venting areas of Rainbow massif. The most mineralized samples are characterized by the highest Zn and Cu concentrations and low δ^{66}Zn and δ^{65}Cu. These compositions were modelled through a progressive hydrothermal sulfide precipitation in abyssal serpentinites. Hydrothermal fluid compositions produced during sulfide dissolution in gabbros was modelled using a Rayleigh distillation and a large range of fluid compositions, for which *ab inito* calculations are available. The composition of mineralized serpentinites was then considered to be a binary mixture between serpentinite and gabbro-derived fluids. These modelled were reproduced here for both Zn and Cu isotopes (see Supplementary Material for modelling details). Both Zn and Cu data set of slow-spreading ridge serpentinites can be explained by the percolation of $Zn(HS)_2(H_2O)_4$ and $Cu(HS)_2(H_2O)_3$ fluids at temperatures ranging from 100 °C to 300 °C. The S-bearing complex give the best match with the slow-spreading ridge dataset relative to other considered complexes (i.e., H_2O-, C- or Cl-bearing complex, Fig. S6). The percolation of either Cl-rich or C-rich fluids will drive abyssal serpentinites either toward heavier or lighter values (Fig. S6) and cannot be invoked to explained the observed Zn and Cu isotope variations. The combination of both Zn and Cu systematics in abyssal serpentinites therefore highlight the circulation of different serpentinizing fluids according to the geodynamic settings, with ultra-slow spreading ridge environments being dominated by seawater like fluids while fluids circulating at slow-spreading ridges are doped in H_2S through gabbros/seawater interactions.

7. Conclusions and perspectives

This review highlights major chemical variations in abyssal serpentinites according to the geodynamical setting and the tectonic context. The major element and REE patterns of abyssal serpentinites is first controlled by melt extraction and melt/rock interaction affecting peridotite composition prior its serpentinization. At fast, slow- and fast-spreading ridges and forearc settings, peridotites are intensively affected by melting processes and magmatic extraction prior their serpentinization. As a consequence, these abyssal serpentinites display low Al_2O_3/SiO_2 and high MgO/SiO_2 ratios (Fig. 5) relative to abyssal serpentinites generated at ultra-slow spreading ridges or transformed faults, where magmatic extraction is limited.

The thermal regimes of the ridges, also related to the abundance of magmatic rocks, play a role on trace element abundance and mobility in fluids, resulting in contrasting mobility of LREE, redox sensitive elements (U, Eu, Ce, As, Sb) and metals (Zn, Cu) in fluids. At ultra-slow spreading ridges or near transform fault, the low magmatic and high tectonic activity lead to the percolation of seawater derived fluids at depth with limited geochemical exchanges with high temperature mafic rocks. The relatively oxidizing conditions of seawater favour Ce immobility in fluids (Fig. 8), the preferential mobility of Sb(V) over Sb(III) (coupled behaviour between Sb and As Fig. 9), as well as the formation of Fe^{3+}-serpentine (Fig. 2) and the storage of sulfate over sulfides in abyssal serpentinites (Fig. 3). These processes favour an extensive leaching of metals results in a decrease of Cu and Zn concentrations and an increase of δ^{65}Cu and δ^{66}Zn values in abyssal serpentinites relative to mantle peridotites.

At slow-spreading ridges the serpentinizing fluid composition is affected by high temperature interactions with gabbros prior serpentinization. These are expected to be equilibrated at high aH_2S and lower fO_2 than pure seawater, as attested by the preferential mobility of Eu^{2+} and Ce^{2+} in fluids (leading to positive Eu and no Ce anomalies, Fig. 8) and by the formation of sulfur and metal (As, Sb, Zn, Cu) -rich serpentinites equilibrated with H_2S fluids (Figs. 10). These fluids are also expected to exert a strong control on redox sensitive mobility favouring As mobility over Sb (Fig. 9) and on the assemblages crystallizing in serpentinites, e.g., favouring the formation of magnetite over Fe^{3+}-serpentine (Fig. 2) and sulfides over sulfate (Fig. 3).

Fast spreading ridge serpentinites display a bimodal distribution of trace element patterns, with samples having a seawater like signature (negative Ce*) and others with a gabbroic signature (positive Eu*). This suggest a two stage serpentinization in this setting, starting nearby the ridge centre at high temperature, probably enhanced by seawater circulation in the lower oceanic crust, and ending off axis nearby fault areas.

Both passive margin and forearc serpentinites are free of Ce anomalies and only few forearc samples display Eu anomalies with moderate LREE enrichments. The forearc serpentinites clearly appear as a geochemical endmember. There, the influence of slab derived fluids enhances the formation of FME element rich serpentinites with a strong affinity with CO_2-rich sediment derived fluids (i.e., enrichments in Cs and As relative to Rb and Sb respectively; Fig. 9).

Surprisingly, the behaviour of fluid mobile and non-redox sensitive elements (e.g., Cs, Ba, Rb, B or Li) is poorly affected by these processes with abyssal serpentinite displaying a homogeneous record at global scale for these elements. Similarly, carbon concentrations, isotopes and redox state are poorly variable among geodynamical settings and tectonic contexts. Most of abyssal serpentinites are characterized by a $[C_{TIC}]/[C_{TC}]$ of about 63 % with passive margin serpentinites characterized by a high TIC abundance relative to other geodynamical settings. The carbon dataset is however affected by sample bias link to limited access to the deepest part of the lithosphere in which TIC is likely to decrease, while abiotic organic carbon is likely stable and might represent a significant, although unconstrained, reservoir of carbon.

Our observations also suggest that the geodynamical settings influence Fe oxidation processes and, therefore, H_2 production at mid-oceanic ridges. Iron oxidation state in abyssal serpentinites is primarily distributed along a serpentinization gradient affecting the oceanic lithosphere with depth. Shallow and highly serpentinized peridotites sampled near the seafloor, often over represented during ocean cruise sampling, display high $Fe^{3+}/\sum Fe$ ratios. In contrast, slightly serpentinized peridotites expected to compose the deep part of the lithosphere are poorly sampled. By comparison with on land ophiolites, these rocks are expected to display relatively low $Fe^{3+}/\sum Fe$ (Fig. 2). This distribution suggests the existence of a redox gradient mainly controlled by the serpentinization degree of oceanic lithosphere. Comparing $Fe^{3+}/\sum Fe$ in serpentinites from different settings, it clearly appears that serpentinites from ultra-slow spreading ridges display higher $Fe^{3+}/\sum Fe$ than serpentinites from passive margin or forearc setting (Fig. 2), while serpentinites from slow spreading ridges and transform faults have intermediate $Fe^{3+}/\sum Fe$, close to that of magnetite. This distribution is also varying with MgO/SiO_2 ratios (Fig. 5), suggesting that high MgO contents, favouring the formation of brucite, is a hindrance to Fe oxidation and H_2 production.

Declaration of competing interest

The authors declare that they have no known competing financial interests or personal relationships that could have appeared to influence the work reported in this paper.

Data availability

Data are provided in supplementary materials

Acknowledgments

This study was supported by the Agence Nationale de la Recherche (ANR) CARBioNic "ANR-22-CE49-0001-01" and DYHAM "ANR-23-CE01-0011-01". We thank Jie Chen for the Spilhaus projection map. We thank three anonymous reviewer for critical comments on earlier version of this article and careful editorial handling by Arturo Gomez-Tuena. This research used samples provided by the IODP and ODP. We are grateful to the crew of the D/V JOIDES Resolution and to the science party of IODP Expedition 366.

Appendix A. Supplementary data

Supplementary data to this article can be found online at https://doi.org/10.1016/j.earscirev.2024.104910.

References

Abers, G.A., Van Keken, P.E., Hacker, B.R., 2017. The cold and relatively dry nature of mantle forearcs in subduction zones. Nat. Geosci. 10, 333–337.
Agrinier, P., Cannat, M., 1997. Oxygen-isotope constraints on serpentinization processes in ultramafic rocks from the Mid-Atlantic Ridge (23N). Proc. Ocean Drill. Program Sci. Results 47, 91–95.
Agrinier, P., Mével, C., Girardeau, J., 1988. Hydrothermal alteration of the peridotites cored at the ocean/continent boundary of the Iberian margin: petrologic and stable isotope evidence. In: Boillot, G., Winterer, E.L., et al. (Eds.), Proc. ODP, Sci. Results, pp. 225–234.
Agrinier, P., Hékinian, R., Bideau, D., Javoy, M., 1995. O and H stable isotope compositions of oceanic crust and upper mantle rocks exposed in the Hess Deep near the Galapagos Triple Junction. Earth Planet. Sci. Lett. 136, 183–196.
Albers, E., Bach, W., Pérez-Gussinyé, M., McCammon, C., Frederichs, T., 2021. Serpentinization-driven H2 production from continental break-up to mid-ocean ridge spreading: unexpected high rates at the West Iberia margin. Front. Earth Sci. 9, 673063.
Allen, D.E., Seyfried Jr., W.E., 2005. REE controls in ultramafic hosted MOR hydrothermal systems: an experimental study at elevated temperature and pressure. Geochim. Cosmochim. Acta 69, 675–683.
Alt, J.C., Shanks, W.C., 1998. Sulfur in serpentinized oceanic peridotites: Serpentinization processes and microbial sulfate reduction. J. Geophys. Res. Solid Earth 103, 9917–9929. https://doi.org/10.1029/98jb00576.
Alt, J.C., Shanks, W.C., 2003. Serpentinization of abyssal peridotites from the MARK area, Mid-Atlantic Ridge: Sulfur geochemistry and reaction modeling. Geochim. Cosmochim. Acta 67, 641–653. https://doi.org/10.1016/S0016-7037(02)01142-0.
Alt, J.C., Shanks, W.C., 2006. Stable isotope compositions of serpentinite seamounts in the Mariana forearc: serpentinization processes, fluid sources and sulfur metasomatism. Earth Planet. Sci. Lett. 242, 272–285.
Alt, J.C., Shanks, W.C., Bach, W., Paulick, H., Garrido, C.J., Beaudoin, G., 2007. Hydrothermal alteration and microbial sulfate reduction in peridotite and gabbro exposed by detachment faulting at the Mid-Atlantic Ridge, 15°20′N (ODP Leg 209): a sulfur and oxygen isotope study. Geochem. Geophys. Geosyst. 8 https://doi.org/10.1029/2007GC001617.
Alt, J.C., Schwarzenbach, E.M., Früh-Green, G.L., Shanks, W.C., Bernasconi, S.M., Garrido, C.J., Crispini, L., Gaggero, L., Padrón-navarta, J.A., Marchesi, C., 2013. The role of serpentinites in cycling of carbon and sulfur : Seafloor serpentinization and subduction metamorphism. Lithos 178, 40–54. https://doi.org/10.1016/j.lithos.2012.12.006.
Andreani, M., Ménez, B., 2020. New perspectives on abiotic organic synthesis and processing during hydrothermal alteration of the oceanic lithosphere. In: Orcutt, B., Daniel, I., Dasgupta, R. (Eds.), Deep Carbon: Past to Present. Cambridge University Press, UK, pp. 447–479. https://doi.org/10.1017/9781108677950.
Andreani, M., Mével, C., Boullier, A.M., Escartín, J., 2007. Dynamic control on serpentine crystallization in veins: Constraints on hydration processes in oceanic peridotites. Geochem. Geophys. Geosyst. 8 https://doi.org/10.1029/2006GC001373.
Andreani, M., Muñoz, M., Marcaillou, C., Delacour, A., 2013. μXANES study of iron redox state in serpentine during oceanic serpentinization. Lithos 178, 70–83. https://doi.org/10.1016/j.lithos.2013.04.008.
Andreani, M., Escartin, J., Delacour, A., Ildefonse, B., Godard, M., Dyment, J., Fallick, A., Fouquet, Y., 2014. Tectonic structure, lithology, and hydrothermal signature of the Rainbow massif (Mid-Atlantic Ridge 36°14'N). Geochem. Geophys. Geosyst. 1–29. https://doi.org/10.1002/2014GC005269.Received.
Andreani, M., Montagnac, G., Fellah, C., Hao, J., Vandier, F., Daniel, I., Pisapia, C., Galipaud, J., Lilley, M.D., Früh Green, G.L., et al., 2023. The rocky road to organics needs drying. Nat. Commun. 14, 347.
Arai, S., Matsukage, K., 1996. Petrology of gabbro-troctolite-peridotite complex from Hess Deep, equatorial Pacific: Implications for mantle-melt interaction within the oceanic lithosphere. In: Proceedings-Ocean Drilling Program Scientific Results, pp. 135–156.
Augustin, N., Lackschewitz, K.S., Kuhn, T., Devey, C.W., 2008. Mineralogical and chemical mass changes in mafic and ultramafic rocks from the Logatchev hydrothermal field (MAR 15°N). Mar. Geol. 256, 18–29. https://doi.org/10.1016/j.margeo.2008.09.004.
Augustin, N., Paulick, H., Lackschewitz, K.S., Eisenhauer, A., Garbe-Schönberg, D., Kuhn, T., Botz, R., Schmidt, M., 2012. Alteration at the ultramafic-hosted Logatchev hydrothermal field: Constraints from trace element and Sr-O isotope data. Geochem. Geophys. Geosyst. 13, 1–20. https://doi.org/10.1029/2011GC003903.
Bach, W., Garrido, C.J., Paulick, H., Harvey, J., Rosner, M., 2004. Seawater-peridotite interactions: First insights from ODP Leg 209, MAR 15 N. Geochem. Geophys. Geosyst. 5.
Barnes, I., O'neil, J.R., Trescases, J.-J., 1978. Present day serpentinization in New Caledonia, Oman and Yugoslavia. Geochim. Cosmochim. Acta 42, 144–145.
Bayrakci, G., Minshull, T.A., Sawyer, D.S., Reston, T.J., Klaeschen, D., Papenberg, C., Ranero, C., Bull, J.M., Davy, R.G., Shillington, D.J., et al., 2016. Fault-controlled hydration of the upper mantle during continental rifting. Nat. Geosci. 9, 384–388.
Beslier, M.O., Ask, M., Boillot, G., 1993. Ocean-continent boundary in the Iberia Abyssal Plain from multichannel seismic data. Tectonophysics 218, 383–393. https://doi.org/10.1016/0040-1951(93)90327-G.
Birner, S.K., Warren, J.M., Cottrell, E., Davis, F.A., Kelley, K.A., Falloon, T.J., 2017. Forearc peridotites from Tonga record heterogeneous oxidation of the mantle following subduction initiation. J. Petrol. 58, 1755–1780.
Blackman, D.K., Canales, J.P., Harding, A., 2009. Geophysical signatures of oceanic core complexes. Geophys. J. Int. 178, 593–613.
Bodinier, J.L., Godard, M., 2013. Orogenic, ophiolitic, and abyssal peridotites, 3rd ed. In: Treatise on Geochemistry, Second edition. Elsevier Ltd. https://doi.org/10.1016/B978-0-08-095975-7.00204-7.
Boillot, G., Grimaud, S., Mauffret, A., Mougenot, D., Kornprobst, J., Mergoil-Daniel, J., Torrent, G., 1980. Ocean-continent boundary off the Iberian margin: a serpentinite diapir west of the Galicia Bank. Earth Planet. Sci. Lett. 48, 23–34. https://doi.org/10.1016/0012-821X(80)90166-1.
Bonatti, E., Crane, K., 1984. Oceanic fracture zones. Sci. Am. 250, 40–51.
Bonatti, E., Ligi, M., Gasperini, L., Peyve, A., Raznitsin, Y.U., Chen, Y.J., 1994. Transform migration and vertical tectonics at the Romanche fracture zone, equatorial Atlantic. J. Geophys. Res. Solid Earth 99, 21779–21802.
Bonatti, E., Brunelli, D., Fabretti, P., Ligi, M., Portaro, R.A., Seyler, M., 2001. Steady-state creation of crust-free lithosphere at cold spots in mid-ocean ridges. Geology 29, 979–982.
Bonatti, E., Brunelli, D., Buck, W.R., Cipriani, A., Fabretti, P., Ferrante, V., Gasperini, L., Ligi, M., 2005. Flexural uplift of a lithospheric slab near the Vema transform (Central Atlantic): timing and mechanisms. Earth Planet. Sci. Lett. 240, 642–655.
Bonnemains, D., Carlut, J., Escartín, J., Mével, C., Andreani, M., Debret, B., 2016. Magnetic signatures of serpentinization at ophiolite complexes. Geochem. Geophys. Geosyst. 17 https://doi.org/10.1002/2016GC006321.
Boschi, C., Früh-Green, G.L., Escartín, J., 2006. Occurrence and significance of serpentinite-hosted, talc- and amphibole-rich fault rocks in modern oceanic settings and ophiolite complexes: an overview. Ofioliti 31, 129–140.
Boschi, C., Dini, A., Früh-Green, G.L., Kelley, D.S., 2008. Isotopic and element exchange during serpentinization and metasomatism at the Atlantis Massif (MAR 30°N): Insights from B and Sr isotope data. Geochim. Cosmochim. Acta 72, 1801–1823. https://doi.org/10.1016/j.gca.2008.01.013.
Boschi, C., Bonatti, E., Ligi, M., Brunelli, D., Cipriani, A., Dallai, L., D'Orazio, M., Früh-Green, G.L., Tonarini, S., Barnes, J.D., Bedini, R.M., 2013. Serpentinization of mantle peridotites along an uplifted lithospheric section, mid Atlantic ridge at 11° N. Lithos 178, 3–23. https://doi.org/10.1016/j.lithos.2013.06.003.
Bouilhol, P., Debret, B., Inglis, E., Burton, K.W., Warembourg, M., Grocolas, T., Rigaudier, T., Villeneuve, J., 2022. Decoupling of inorganic and organic carbon during slab mantle devolatilisation. Nat. Commun. 13, 308. https://doi.org/10.1038/s41467-022-27970-0.
Bown, J.W., White, R.S., 1994. Variation with spreading rate of oceanic crustal thickness and geochemistry. Earth Planet. Sci. Lett. 121, 435–449.
Breuer, C., Pichler, T., 2013. Arsenic in marine hydrothermal fluids. Chem. Geol. 348, 2–14.
Canales, J.P., Collins, J.A., Escartín, J., Detrick, R.S., 2000. OF GEOPHYSICAL Seismic structure across the rift valley of the processes at slow spreading ridges the results from seismic profile across the rift valley of the of the models Snake Pit are consistent with elevated axial temperatures and with the presence. J. Geophys. Res. E Planets 105, 28,411–28,425.
Canil, D., O'Neill, H.S.C., Pearson, D.G., Rudnick, R.L., McDonough, W.F., Carswell, D.A., 1994. Ferric iron in peridotites and mantle oxidation states. Earth Planet. Sci. Lett. 123, 205–220. https://doi.org/10.1016/0012-821X(94)90268-2.
Cannaò, E., Malaspina, N., 2018. From oceanic to continental subduction: Implications for the geochemical and redox evolution of the supra-subduction mantle. Geosphere 14, 2311–2336. https://doi.org/10.1130/GES01597.1.
Cannat, M., 1995. Thin crust, ultramafic exposures, and rugged faulting patterns at the Mid-Atlantic Ridge (22°-24°N). Geology 23, 49–52. https://doi.org/10.1130/0091-7613(1995)023<0049:TCUEAR>2.3.CO;2.
Cannat, M., Sauter, D., Mendel, V., Ruellan, E., Okino, K., Escartin, J., Combier, V., Baala, M., 2006. Modes of seafloor generation at a melt-poor ultraslow-spreading ridge. Geology 34, 605–608.

Cannat, M., Sauter, D., Bezos, A., Meyzen, C., Humler, E., Le Rigoleur, M., 2008. Spreading rate, spreading obliquity, and melt supply at the ultraslow spreading Southwest Indian Ridge. Geochem. Geophys. Geosyst. 9.

Carignan, J., Hild, P., Mevelle, G., Morel, J., Yeghicheyan, D., 2001. Routine analyses of trace elements in geological samples using flow injection and low pressure on-line liquid chromatography coupled to ICP-MS: A study of geochemical reference materials BR, DR-N, UB-N, AN-G and GH. Geostand. Newsl. 25, 187–198. https://doi.org/10.1111/j.1751-908x.2001.tb00595.x.

Charlou, J.L., Donval, J.P., Fouquet, Y., Jean-baptiste, P., Holm, N., 2002. Geochemistry of high H2 and CH4 vent fluids issuing from ultramafic rocks at the Rainbow hydrothermal field (36°14′ N, MAR). Chem. Geol. 191, 345–359. https://doi.org/10.1016/S0009-2541(02)00134-1.

Chaussidon, M., Albarède, F., Sheppard, S.M.F., 1989. Sulphur isotope variations in the mantle from ion microprobe analyses of micro-sulphide inclusions. Earth Planet. Sci. Lett. 92, 144–156. https://doi.org/10.1016/0012-821X(89)90042-3.

Chen, J., Zhang, T., Tominaga, M., Escartin, J., Kang, R., 2023. Ocean sciences with the spilhaus projection: a seamless ocean map for spatial data recognition. Sci. Data 10, 410.

Coleman, R.G., Keith, T.E., 1971. A chemical study of serpentinization—Burro Mountain, California. J. Petrol. 12, 311–328.

Corbalán, A., Nedimović, M.R., Louden, K.E., Cannat, M., Grevemeyer, I., Watremez, L., Leroy, S., 2021. Seismic velocity structure along and across the ultraslow-spreading Southwest Indian Ridge at 64° 30′ E showcases flipping detachment faults. J. Geophys. Res. Solid Earth 126, e2021JB022177.

Craddock, P.R., Warren, J.M., Dauphas, N., 2013. Abyssal peridotites reveal the near-chondritic Fe isotopic composition of the Earth. Earth Planet. Sci. Lett. 365, 63–76. https://doi.org/10.1016/j.epsl.2013.01.011.

Craig, T.J., Parnell-Turner, R., 2017. Depth-varying seismogenesis on an oceanic detachment fault at 13° 20′ N on the Mid-Atlantic Ridge. Earth Planet. Sci. Lett. 479, 60–70.

Dasgupta, R., Hirschmann, M.M., 2010. The deep carbon cycle and melting in Earth's interior. Earth Planet. Sci. Lett. 298, 1–13. https://doi.org/10.1016/j.epsl.2010.06.039.

Dauphas, N., John, S.G., Rouxel, O., 2017. Iron isotope systematics. Non-Traditional Stable Isot. 82, 415–510. https://doi.org/10.2138/rmg.2017.82.11.

Day, J.M.D., Brown, D.B., 2021. Ancient melt-depletion in fresh to strongly serpentinized Tonga trench peridotites. J. Petrol. 62, egab088.

Day, J.M.D., Walker, R.J., Warren, J.M., 2017. 186Os–187Os and highly siderophile element abundance systematics of the mantle revealed by abyssal peridotites and Os-rich alloys. Geochim. Cosmochim. Acta 200, 232–254.

Debret, B., Sverjensky, D.A., 2017. Highly oxidising fluids generated during serpentinite breakdown in subduction zones. Sci. Rep. 7, 10351. https://doi.org/10.1038/s41598-017-09626-y.

Debret, B., Andreani, M., Godard, M., Nicollet, C., Schwartz, S., Lafay, R., 2013a. Trace element behavior during serpentinization/de-serpentinization of an eclogitized oceanic lithosphere: a LA-ICPMS study of the Lanzo ultramafic massif (Western Alps). Chem. Geol. 357, 117–133. https://doi.org/10.1016/j.chemgeo.2013.08.025.

Debret, B., Nicollet, C., Andreani, M., Schwartz, S., Godard, M., 2013b. Three steps of serpentinization in an eclogitized oceanic serpentinization front (Lanzo Massif - Western Alps). J. Metamorph. Geol. 31, 165–186. https://doi.org/10.1111/jmg.12008.

Debret, B., Andreani, M., Muñoz, M., Bolfan-Casanova, N., Carlut, J., Nicollet, C., Schwartz, S., Trcera, N., 2014. Evolution of Fe redox state in serpentine during subduction. Earth Planet. Sci. Lett. 400, 206–218. https://doi.org/10.1016/j.epsl.2014.05.038.

Debret, B., Andreani, M., Delacour, A., Rouméjon, S., Trcera, N., Williams, H., 2017. Assessing sulfur redox state and distribution in abyssal serpentinites using XANES spectroscopy. Earth Planet. Sci. Lett. 466, 1–11. https://doi.org/10.1016/j.epsl.2017.02.029.

Debret, B., Beunon, H., Mattielli, N., Andreani, M., Ribeiro da Costa, I., Escartin, J., 2018. Ore component mobility, transport and mineralization at mid-oceanic ridges: a stable isotopes (Zn, Cu and Fe) study of the Rainbow massif (Mid-Atlantic Ridge 36°14′N). Earth Planet. Sci. Lett. 503, 170–180. https://doi.org/10.1016/j.epsl.2018.09.009.

Debret, B., Albers, E., Walter, B., Price, R., Barnes, J.D., Beunon, H., Facq, S., Gillikin, D. P., Mattielli, N., Williams, H., 2019. Shallow forearc mantle dynamics and geochemistry: New insights from IODP Expedition 366. Lithos 326, 326–327. https://doi.org/10.1016/j.lithos.2018.10.038.

Debret, B., Reekie, C.D.J., Mattielli, N., Beunon, H., Ménez, B., Savov, I.P., Williams, H. M., 2020. Redox transfer at subduction zones : insights from Fe isotopes in the Mariana forearc. Geochem. Perspect. Lett. 12, 46–51. https://doi.org/10.7185/geochemlet.2003.

Debret, B., Ménez, B., Walter, B., Bouquerel, H., Bouilhol, P., Mattielli, N., Pisapia, C., Rigaudier, T., Williams, H.M., 2022. High-pressure synthesis and storage of solid organic compounds in active subduction zones. Sci. Adv. 8, eabo2397.

Delacour, A., Früh-Green, G.L., Bernasconi, S.M., Kelley, D.S., 2008a. Sulfur in peridotites and gabbros at Lost City (30°N, MAR): Implications for hydrothermal alteration and microbial activity during serpentinization. Geochim. Cosmochim. Acta 72, 5090–5110. https://doi.org/10.1016/j.gca.2008.07.017.

Delacour, A., Früh-Green, G.L., Bernasconi, S.M., Schaeffer, P., Kelley, D.S., 2008b. Carbon geochemistry of serpentinites in the Lost City Hydrothermal System (30 ° N, MAR). Geochim. Cosmochim. Acta 72, 3681–3702. https://doi.org/10.1016/j.gca.2008.04.039.

Deschamps, F., Guillot, S., Godard, M., Andreani, M., Hattori, K., 2011. Serpentinites act as sponges for fluid-mobile elements in abyssal and subduction zone environments. Terra Nova 23, 171–178.

Deschamps, F., Godard, M., Guillot, S., Hattori, K., 2013. Geochemistry of subduction zone serpentinites: a review. Lithos 178, 96–127. https://doi.org/10.1016/j.lithos.2013.05.019.

Dessimoulie, L., 2019. Apports de la géochimie élémentaire et isotopique pour la compréhension des processus de serpentinisation : cas de la dorsale sud-ouest indienne. Université de Lyon. 425 pages. doi:NNT : 2019LYSES013 https://theses.hal.science/tel-02467017v1/file/These-DESSIMOULIE-2019.pdf.

Dessimoulie, L., Delacour, A., Guillaume, D., Chevet, J., Cottin, J.Y., 2020. Major and trace elements exchanges during fluid-rock interaction at ultraslow-spreading oceanic lithosphere: example of the South West Indian Ridge (SWIR). Lithos 352–353. https://doi.org/10.1016/j.lithos.2019.105233.

Ding, T., Tao, C., Dias, Á.A., Liang, J., Chen, J., Wu, B., Ma, D., Zhang, R., Wang, J., Liao, S., et al., 2021. Sulfur isotopic compositions of sulfides along the Southwest Indian Ridge: implications for mineralization in ultramafic rocks. Mineral. Deposita 56, 991–1006.

Douville, E., Charlou, J.L., Oelkers, E.H., Bienvenu, P., Colon, C.F.J., Donval, J.P., Fouquet, Y., Prieur, D., Appriou, P., 2002. The rainbow vent fluids (36 14′ N, MAR): the influence of ultramafic rocks and phase separation on trace metal content in Mid-Atlantic Ridge hydrothermal fluids. Chem. Geol. 184, 37–48.

Drouin, M., Godard, M., Ildefonse, B., Bruguier, O., Garrido, C.J., 2009. Geochemical and petrographic evidence for magmatic impregnation in the oceanic lithosphere at Atlantis Massif, Mid-Atlantic Ridge (IODP Hole U1309D, 30 N). Chem. Geol. 264, 71–88.

Ducher, M., Blanchard, M., Balan, E., 2016. Equilibrium zinc isotope fractionation in Zn-bearing minerals from first-principles calculations. Chem. Geol. 443, 87–96. https://doi.org/10.1016/j.chemgeo.2016.09.016.

Duncan, M.S., Dasgupta, R., 2017. Rise of Earth's atmospheric oxygen controlled by efficient subduction of organic carbon. Nat. Geosci. 10, 387–392. https://doi.org/10.1038/ngeo2939.

Dunn, R.A., Arai, R., Eason, D.E., Canales, J.P., Sohn, R.A., 2017. Three-dimensional seismic structure of the Mid-Atlantic Ridge: an investigation of tectonic, magmatic, and hydrothermal processes in the rainbow area. J. Geophys. Res. Solid Earth 122, 9580–9602.

Dusunur, D., Escart'in, J., Combier, V., Seher, T., Crawford, W., Cannat, M., Singh, S.C., Matias, L.M., Miranda, J.M., 2009. Seismological constraints on the thermal structure along the Lucky strike segment (Mid-Atlantic Ridge) and interaction of tectonic and magmatic processes around the magma chamber. Mar. Geophys. Res. 30, 105–120.

Edwards, S.J., Malpas, J., 1996. Melt-peridotite interactions in shallow mantle at the East Pacific rise: evidence from ODP Site 895 (Hess deep). Mineral. Mag. 60, 191–206.

Eguchi, J., Seales, J., Dasgupta, R., 2020. Deep cycling and enhanced degassing of carbon. Nat. Geosci. 13 https://doi.org/10.1038/s41561-019-0492-6.

Eickmann, B., Bach, W., Rosner, M., Peckmann, J., 2009. Geochemical constraints on the modes of carbonate precipitation in peridotites from the Logatchev Hydrothermal Vent Field and Gakkel Ridge. Chem. Geol. 268, 97–106.

Escartin, J., Canales, J.P., 2011. Detachments in Oceanic Lithosphere: Deformation, Magmatism, Fluid Flow, and Ecosystems.

Escartin, J., Smith, D.K., Cann, J., Schouten, H., Langmuir, C.H., Escrig, S., 2008. Central role of detachment faults in accretion of slow-spreading oceanic lithosphere. Nature 455, 790–794.

Evans, B.W., 2008. Control of the products of serpentinization by the Fe2+ Mg-1 exchange potential of olivine and orthopyroxene. J. Petrol. 49, 1873–1887. https://doi.org/10.1093/petrology/egn050.

Ewans, J., Hawkins, J., 1979. Petrology of "seamounts" on the trench slope break. Eos (Washington. DC). 60, 968.

Ficher, R.L., Engel, C.G., 1969. Ultramafic and basaltic rocks dredged from the near-shore flank of the Tonga trench. GSA Bull. 80, 1373–1378.

Fouquet, Y., Cambon, P., Etoubleau, J., Charlou, J.L., Ondréas, H., Barriga, F.J.A.S., Cherkashov, G., Semkova, T., Poroshina, I., Bohn, M., Al, E., 2010. Geodiversity of hydrothermal processes along the Mid-Atlantic Ridge and ultramafic-hosted mineralization: a new type of oceanic Cu-Zn-Co-Au volcanogenic massive sulfide deposit. Divers. Hydrothermal Syst. Slow Spreading Ocean Ridges 188, 321–367.

Frisby, C., Bizimis, M., Mallick, S., 2016. Seawater-derived rare earth element addition to abyssal peridotites during serpentinization. Lithos 248, 432–454.

Froment, B., McGuire, J.J., Van Der Hilst, R.D., Gouédard, P., Roland, E.C., Zhang, H., Collins, J.A., 2014. Imaging along-strike variations in mechanical properties of the Gofar transform fault, East Pacific Rise. J. Geophys. Res. Solid Earth 119, 7175–7194.

Frost, R.B., Beard, J.S., 2007. On silica activity and serpentinization. J. Petrol. 48, 1351–1368. https://doi.org/10.1093/petrology/egm021.

Früh-Green, G.L., Connolly, J.A.D., Plas, A., Kelley, D.S., Grobéty, B., 2004. Serpentinization of oceanic peridotites: implications for geochemical cycles and biological activity. subseafloor Biosph. mid-ocean ridges 144, 119–136.

Fryer, P., 1996. Evolution of the Mariana convergent plate margin system. Rev. Geophys. 34, 89–125. https://doi.org/10.1029/95RG03476.

Fryer, P., 2012. Serpentinite Mud Volcanism: Observations, Processes, and Implications. Annu. Rev. Mar. Sci. 4, 345–373. https://doi.org/10.1146/annurev-marine-120710-100922.

Fryer, P., Wheat, C.G., Mottl, M.J., 1999. Mariana blueschist mud volcanism: Implications for conditions within the subduction zone. Geology 27, 103–106. https://doi.org/10.1130/0091-7613(1999)027<0103:MBMVIF>2.3.CO;2.

Fujii, T., Moynier, F., Blichert-Toft, J., Albarède, F., 2014. Density functional theory estimation of isotope fractionation of Fe, Ni, Cu, and Zn among species relevant to geochemical and biological environments. Geochim. Cosmochim. Acta 140, 553–576. https://doi.org/10.1016/j.gca.2014.05.051.

Geldmacher, J., Hoernle, K., van den Bogaard, P., Hauff, F., Klügel, A., 2008. Age and geochemistry of the central American forearc basement (DSDP Leg 67 and 84): Insights into mesozoic arc volcanism and seamount accretion on the fringe of the Caribbean LIP. J. Petrol. https://doi.org/10.1093/petrology/egn046.
Godard, M., Jousselin, D., Bodinier, J.L., 2000. Relationships between geochemistry and structure beneath a palaeo-spreading Centre: a study of the mantle section in the Oman ophiolite. Earth Planet. Sci. Lett. 180, 133–148. https://doi.org/10.1016/S0012-821X(00)00149-7.
Godard, M., Lagabrielle, Y., Alard, O., Harvey, J., 2008. Geochemistry of the highly depleted peridotites drilled at ODP Sites 1272 and 1274 (Fifteen-twenty Fracture Zone, Mid-Atlantic Ridge): Implications for mantle dynamics beneath a slow spreading ridge. Earth Planet. Sci. Lett. 267, 410–425. https://doi.org/10.1016/j.epsl.2007.11.058.
Gregg, P.M., Lin, J., Behn, M.D., Montési, L.G.J., 2007. Spreading rate dependence of gravity anomalies along oceanic transform faults. Nature 448, 183–187.
Gregory, E.P.M., Singh, S.C., Marjanović, M., Wang, Z., 2021. Serpentinized peridotite versus thick mafic crust at the Romanche oceanic transform fault. Geology 49, 1132–1136.
Grevemeyer, I., Hayman, N.W., Peirce, C., Schwardt, M., Van Avendonk, H.J.A., Dannowski, A., Papenberg, C., 2018. Episodic magmatism and serpentinized mantle exhumation at an ultraslow-spreading Centre. Nat. Geosci. 11, 444–448.
Grevemeyer, I., Hayman, N.W., Lange, D., Peirce, C., Papenberg, C., Van Avendonk, H.J.A., Schmid, F., de La Peña, L.G., Dannowski, A., 2019. Constraining the maximum depth of brittle deformation at slow-and ultraslow-spreading ridges using microseismicity. Geology 47, 1069–1073.
Guillot, S., Schwartz, S., Reynard, B., Agard, P., Prigent, C., 2015. Tectonic significance of serpentinites. Tectonophysics 646, 1–19. https://doi.org/10.1016/j.tecto.2015.01.020.
Guo, J., Griffin, W.L., O'Reilly, S.Y., 1999. Geochemistry and origin of sulphide minerals in mantle xenoliths: Qilin, Southeastern China. J. Petrol. 40, 1125–1149.
Hattori, K.H., Guillot, S., 2007. Geochemical character of serpentinites associated with high- to ultrahigh-pressure metamorphic rocks in the Alps, Cuba, and the Himalayas: Recycling of elements in subduction zones. Geochem. Geophys. Geosyst. 8 https://doi.org/10.1029/2007GC001594.
Hattori, K., Takahashi, Y., Guillot, S., Johanson, B., 2005. Occurrence of arsenic (V) in forearc mantle serpentinites based on X-ray absorption spectroscopy study. Geochim. Cosmochim. Acta 69, 5585–5596.
Hayman, N.W., Grindlay, N.R., Perfit, M.R., Mann, P., Leroy, S., de Lépinay, B.M., 2011. Oceanic core complex development at the ultraslow spreading Mid-Cayman Spreading Center. Geochem. Geophys. Geosyst. 12.
Hébert, R., Gueddari, K., Lafleche, M.R., Beslier, M.-O., Gardien, V., 2001. Petrology and geochemistry of exhumed peridotites and gabbros at non-volcanic margins: ODP Leg 173 West Iberia ocena-continent transition zone. Geol. Soc. London Spec. Publ. 187, 161–189.
Hedenquist, J.W., Lowenstern, J.B., 1994. The role of magmas in the formation of hydrothermal ore deposits. Nature 370, 519–527.
Hershey, J.P., Fernandez, M., Milne, P.J., Millero, F.J., 1986. The ionization of boric acid in NaCl, Na-Ca-Cl and Na-Mg-Cl solutions at 25° C. Geochim. Cosmochim. Acta 50, 143–148.
Hodel, F., Macouin, M., Triantafyllou, A., Carlut, J., Berger, J., Rousse, S., Ennih, N., Trindade, R.I.F., 2017. Unusual massive magnetite veins and highly altered Cr-spinels as relics of a Cl-rich acidic hydrothermal event in Neoproterozoic serpentinites (Bou Azzer ophiolite, Anti-Atlas, Morocco). Precambrian Res. 300, 151–167. https://doi.org/10.1016/j.precamres.2017.08.005.
Hodel, F., Macouin, M., Trindade, R.I.F., Triantafyllou, A., Ganne, J., Chavagnac, V., Berger, J., Rospabe, M., Destrigneville, C., Carlut, J., et al., 2018. Fossil black smoker yields oxygen isotopic composition of Neoproterozoic seawater. Nat. Commun. 9, 1453.
Hyndman, R.D., Peacock, S.M., 2003. Serpentinization of the forearc mantle. Earth Planet. Sci. Lett. 212, 417–432.
Ildefonse, B., Blackman, D.K., John, B.E., Ohara, Y., Miller, D.J., MacLeod, C.J., 2007. Oceanic core complexes and crustal accretion at slow-spreading ridges. Geology 35, 623–626.
Jagoutz, E., Palme, H., Baddenhausen, H., Blum, K., Cendales, M., Dreibus, G., Spettel, B., Lorenz, V., Wänke, H., 1979. The abundances of major, minor and trace elements in the earth's mantle as derived from primitive ultramafic nodules. In: Lunar and Planetary Science Conference, 10th, Houston, Tex., March 19-23, 1979, Proceedings, Vol. 2. Pergamon Press, Inc, New York, pp. 2031–2050 (A80-23617 08-91). Research Supported by the Deutsche Forschungsgemeinschaft. pp. 2031–2050.
Jochum, K.P., Seufert, H.M., Thirlwall, M.F., 1990. High-sensitivity Nb analysis by spark-source mass spectrometry (SSMS) and calibration of XRF Nb and Zr. Chem. Geol. 81, 1–16.
Jones, L.C., Rosenbauer, R., Goldsmith, J.I., Oze, C., 2010. Carbonate control of H2 and CH4 production in serpentinization systems at elevated P-Ts. Geophys. Res. Lett. 37, 1–6. https://doi.org/10.1029/2010GL043769.
Jöns, N., Bach, W., Klein, F., 2010. Magmatic influence on reaction paths and element transport during serpentinization. Chem. Geol. 274, 196–211. https://doi.org/10.1016/j.chemgeo.2010.04.009.
Kelemen, P.B., Manning, C.E., 2015. Reevaluating carbon fluxes in subduction zones, what goes down, mostly comes up. Proc. Natl. Acad. Sci. USA 112, 3997–4006. https://doi.org/10.1073/pnas.1507889112.
Kelley, D.S., Karson, J.A., Fruh-Green, G.L., Yoerger, D.R., Shank, T.M., Butterfield, D.A., Hayes, J.M., Schrenk, M.O., Olson, E.J., Proskurowski, G., Jakuba, M., Bradley, A.S., Larson, B., Ludwig, K., Glickson, D., Buckman, K., Brazelton, W.J., Roe, K., Bernasconi, S.M., Elend, M.J., Lilley, M.D., Baross, J.A., Summons, R.E., Sylva, S.P., 2005. A serpentinite-hosted ecosystem: the lost city hydrothermal field. Science 307, 1428–1434. https://doi.org/10.1126/science.1102556.
Klein, F., Bach, W., 2009. Fe-Ni-Co-O-S phase relations in peridotite-seawater interactions. J. Petrol. 50, 37–59. https://doi.org/10.1093/petrology/egn071.
Klein, F., Bach, W., McCollom, T.M., 2013. Compositional controls on hydrogen generation during serpentinization of ultramafic rocks. Lithos 178, 55–69.
Klein, F., Bach, W., Humphris, S.E., Kahl, W.A., Jöns, N., Moskowitz, B., Berquó, T.S., 2014. Magnetite in seafloor serpentinite-Some like it hot. Geology 42, 135–138. https://doi.org/10.1130/G35068.1.
Kodolányi, J., Pettke, T., Spandler, C., Kamber, B.S., Ling, K.G., 2012. Geochemistry of ocean floor and fore-arc serpentinites: Constraints on the ultramafic input to subduction zones. J. Petrol. 53, 235–270. https://doi.org/10.1093/petrology/egr058.
Komor, S.C., Elthon, D., Casey, J.F., 1985. Serpentinization of cumulate ultramafic rocks from the North arm Mountain massif of the Bay of Islands ophiolite. Geochim. Cosmochim. Acta 49, 2331–2338.
Lafay, R., Montes-Hernandez, G., Janots, E., Munoz, M., Auzende, A.L., Gehin, A., Chiriac, R., Proux, O., 2016. Experimental investigation of As, Sb and Cs behavior during olivine serpentinization in hydrothermal alkaline systems. Geochim. Cosmochim. Acta 179, 177–202.
Lafay, R., Baumgartner, L.P., Schwartz, S., Picazo, S., Montes Hernandez, G., Vennemann, T., 2017. Petrologic and stable isotopic studies of a fossil hydrothermal system in ultramafic environment (Chenaillet ophicalcites, Western Alps, France): Processes of carbonate cementation. Lithos 294–295, 319–338. https://doi.org/10.1016/j.lithos.2017.10.006.
Lecoeuvre, A., Ménez, B., Cannat, M., Chavagnac, V., Gérard, E., 2021. Microbial ecology of the newly discovered serpentinite-hosted Old City hydrothermal field (southwest Indian ridge). ISME J. 15, 818–832.
Li, Y.-H., 1991. Distribution patterns of the elements in the ocean: a synthesis. Geochim. Cosmochim. Acta 55, 3223–3240.
Liu, S.-A., Liu, P.-P., Lv, Y., Wang, Z.-Z., Dai, J.-G., 2019. Cu and Zn isotope fractionation during oceanic alteration: Implications for Oceanic Cu and Zn cycles. Geochim. Cosmochim. Acta 257, 191–205.
Liu, S., Li, Y., Liu, Jie, Yang, Z., Liu, Jianming, Shi, Y., 2021. Equilibrium Cu isotope fractionation in copper minerals: a first-principles study. Chem. Geol. 564, 120060.
MacLeod, C.J., Searle, R.C., Murton, B.J., Casey, J.F., Mallows, C., Unsworth, S.C., Achenbach, K.L., Harris, M., 2009. Life cycle of oceanic core complexes. Earth Planet. Sci. Lett. 287, 333–344.
Maffione, M., Morris, A., Plümper, O., Van Hinsbergen, D.J.J., 2014. Magnetic properties of variably serpentinized peridotites and their implication for the evolution of oceanic core complexes. Geochem. Geophys. Geosyst. 15, 923–944.
Maia, M., Brunelli, D., Ligi, M., 2019. SMARTIES cruise, RV Pourquoi pas ? https://doi.org/10.17600/18001107.
Malvoisin, B., 2015. Mass transfer in the oceanic lithosphere: Serpentinization is not isochemical. Earth Planet. Sci. Lett. 430, 75–85. https://doi.org/10.1016/j.epsl.2015.07.043.
Marschall, H.R., 2018. Boron isotopes in the ocean floor realm and the mantle. Boron Isot. fifth Elem. 189–215.
Martin, B., Fyfe, W.S., 1970. Some experimental and theoretical observations on the kinetics of hydration reactions with particular reference to serpentinization. Chem. Geol. 6, 185–202.
McCaig, A.M., Delacour, A., Fallick, A.E., Castelain, T., Früh-Green, G.L., 2010. Detachment fault control on hydrothermal circulation systems: Interpreting the subsurface beneath the TAG hydrothermal field using the isotopic and geological evolution of oceanic core complexes in the Atlantic. Divers. Hydrothermal. Syst. Slow Spread. Ocean Ridges, Geophys. Monogr. Ser 188, 207–240.
McCollom, T.M., Bach, W., 2009. Thermodynamic constraints on hydrogen generation during serpentinization of ultramafic rocks. Geochim. Cosmochim. Acta 73, 856–875.
McCollom, T.M., Klein, F., Moskowitz, B., Berquó, T.S., Bach, W., Templeton, A.S., 2020. Hydrogen generation and iron partitioning during experimental serpentinization of an olivine–pyroxene mixture. Geochim. Cosmochim. Acta 282, 55–75. https://doi.org/10.1016/j.gca.2020.05.016.
McDonough, W.F., Sun, S.-S., 1995. The composition of the Earth. Chem. Geol. 120, 223–253.
Ménez, B., Pasini, V., Brunelli, D., 2012. Life in the hydrated suboceanic mantle. Nat. Geosci. 5, 133–137. https://doi.org/10.1038/ngeo1359.
Ménez, B., Pisapia, C., Andreani, M., Jamme, F., Vanbellingen, Q.P., Brunelle, A., Richard, L., Dumas, P., Réfrégiers, M., 2018. Abiotic synthesis of amino acids in the recesses of the oceanic lithosphere. Nature 564, 59–63. https://doi.org/10.1038/s41586-018-0684-z.
Mével, C., 2003. Serpentinisation des péridotites abysales aux dorsales océaniques. Compt. Rendus Geosci. 335, 825–852. https://doi.org/10.1016/j.crte.2003.08.006.
Mével, C., Stamoudi, C., 1996. 15. HYDROTHERMAL ALTERATION OF THE UPPER-MANTLE SECTION AT HESS DEEP1. In: Proceedings of THE Ocean Drilling Program, Scientific Results.
Milliken, K.L., Lynch, F.L., Seifert, K.E., 1996. Marine weathering of serpentinites and serpentinite breccias, sites 897 and 899, Iberia Abyssal Plain. In: Proceedings-Ocean Drilling Program Scientific Results, pp. 529–540.
Minshull, T.A., 2009. Geophysical characterisation of the ocean-continent transition at magma-poor rifted margins. Compt. Rendus Geosci. 341, 382–393. https://doi.org/10.1016/j.crte.2008.09.003.
Miranda, E.A., John, B.E., 2010. Strain localization along the Atlantis Bank oceanic detachment fault system, Southwest Indian Ridge. Geochem. Geophys. Geosyst. 11.
Mothersole, F.E., Evans, K., Frost, B.R., 2017. Abyssal and hydrated mantle wedge serpentinised peridotites: a comparison of the 15 ∘ 20 ′ N fracture zone and New

Caledonia serpentinites. Contrib. Mineral. Petrol. 172 https://doi.org/10.1007/s00410-017-1381-x.
Moynier, F., Vance, D., Fujii, T., Savage, P., 2017. The isotope geochemistry of zinc and copper. Non-Traditional Stable Isot. 82, 543–600. https://doi.org/10.2138/rmg.2017.82.13.
Niu, Y., 1997. Mantle melting and melt extraction processes beneath ocean ridges: evidence from abyssal peridotites. J. Petrol. 38, 1047–1074.
Niu, Y., 2004. Bulk-rock major and trace element compositions of abyssal peridotites: Implications for mantle melting, melt extraction and post-melting processes beneath Mid-Ocean ridges. J. Petrol. 45, 2423–2458. https://doi.org/10.1093/petrology/egh068.
Noël, J., Godard, M., Oliot, E., Martinez, I., Williams, M., Boudier, F., Rodriguez, O., Chaduteau, C., Escario, S., Gouze, P., 2018. Evidence of polygenetic carbon trapping in the Oman Ophiolite: Petro-structural, geochemical, and carbon and oxygen isotope study of the Wadi Dima harzburgite-hosted carbonates (Wadi Tayin massif, Sultanate of Oman). Lithos 323, 218–237.
Och, L.M., Shields-Zhou, G.A., 2012. The Neoproterozoic oxygenation event: Environmental perturbations and biogeochemical cycling. Earth-Sci. Rev. 110, 26–57. https://doi.org/10.1016/j.earscirev.2011.09.004.
O'Hanley, D.S., 1996. Serpentinites: Records of Tectonic and Petrological History. Oxford University Press on Demand.
Paquet, M., Day, J.M.D., Brown, D.B., Waters, C.L., 2022. Effective global mixing of the highly siderophile elements into Earth's mantle inferred from oceanic abyssal peridotites. Geochim. Cosmochim. Acta 316, 347–362. https://doi.org/10.1016/j.gca.2021.09.033.
Parkinson, I.J., Pearce, J.A., 1998. Peridotites from the Izu-Bonin-Mariana forearc (ODP Leg 125): evidence for mantle melting and melt-mantle interaction in a supra-subduction zone setting. J. Petrol. 39, 1577–1618. https://doi.org/10.1093/petroj/39.9.1577.
Parnell-Turner, R., Sohn, R.A., Peirce, C., Reston, T.J., MacLeod, C.J., Searle, R.C., Simão, N.M., 2021. Seismicity trends and detachment fault structure at 13 N, Mid-Atlantic Ridge. Geology 49, 320–324.
Pasini, V., Brunelli, D., Dumas, P., Sandt, C., Frederick, J., Benzerara, K., Bernard, S., Ménez, B., 2013. Low temperature hydrothermal oil and associated biological precursors in serpentinites from mid-ocean ridge. Lithos 178, 84–95. https://doi.org/10.1016/j.lithos.2013.06.014.
Paulick, H., Bach, W., Godard, M., de Hoog, C.-J., Suhr, G., Harvey, J., 2006. ODP Leg 209: Implications for fluid / rock interaction in slow spreading environments. Chem. Geol. 234, 179–210. https://doi.org/10.1016/j.chemgeo.2006.04.011.
Pearce, J.A., Barker, P.F., Edwards, S.J., Parkinson, I.J., Leat, P.T., 2000. Geochemistry and tectonic significance of peridotites from the South Sandwich arc-basin system, South Atlantic. Contrib. Mineral. Petrol. 139, 36–53. https://doi.org/10.1007/s004100050572.
Pens, M., Andreani, M., Daniel, I., Perrillat, J.P., Cardon, H., 2016. Contrasted effect of aluminum on the serpentinization rate of olivine and orthopyroxene under hydrothermal conditions. Chem. Geol. 441, 256–264. https://doi.org/10.1016/j.chemgeo.2016.08.007.
Pérez-Gussinyé, M., Reston, T.J., 2001. Rheological evolution during extension at nonvolcanic rifted margins: Onset of serpentinization and development of detachments leading to continental breakup. J. Geophys. Res. Solid Earth 106, 3961–3975.
Peters, D., Bretscher, A., John, T., Scambelluri, M., Pettke, T., 2017. Fluid-mobile elements in serpentinites: Constraints on serpentinisation environments and element cycling in subduction zones. Chem. Geol. 466, 654–666. https://doi.org/10.1016/j.chemgeo.2017.07.017.
Pettke, T., Bretscher, A., 2022. Fluid-mediated element cycling in subducted oceanic lithosphere: the orogenic serpentinite perspective. Earth-Sci. Rev. 225, 103896. https://doi.org/10.1016/j.earscirev.2021.103896.
Picazo, S., Cannat, M., Delacour, A., Escart'in, J., Rouméjon, S., Silantyev, S., 2012. Deformation associated with the denudation of mantle-derived rocks at the Mid-Atlantic Ridge 13°–15° N: The role of magmatic injections and hydrothermal alteration. Geochem. Geophys. Geosyst. 13.
Piccardo, G.B., Zanetti, A., Müntener, O., 2007. Melt/peridotite interaction in the Southern Lanzo peridotite: Field, textural and geochemical evidence. Lithos 94, 181–209. https://doi.org/10.1016/j.lithos.2006.07.002.
Pickle, R.C., Forsyth, D.W., Harmon, N., Nagle, A.N., Saal, A., 2009. Thermo-mechanical control of axial topography of intra-transform spreading centers. Earth Planet. Sci. Lett. 284, 343–351.
Plank, T., Manning, C.E., 2019. Subducting carbon. Nature 574, 343–352. https://doi.org/10.1038/s41586-019-1643-z.
Polyakov, V.B., Mineev, S.D., 2000. The use of Mossbauer spectroscopy in stable isotope geochemistry. Geochim. Cosmochim. Acta 64, 849–865. https://doi.org/10.1016/S0016-7037(99)00329-4.
Pons, M.-L., Quitte, G., Fujii, T., Rosing, M.T., Reynard, B., Moynier, F., Douchet, C., Albarede, F., 2011. Early Archean serpentine mud volcanoes at Isua, Greenland, as a niche for early life. Proc. Natl. Acad. Sci. 108, 17639–17643. https://doi.org/10.1073/pnas.1108061108.
Prigent, C., Warren, J.M., Kohli, A.H., Teyssier, C., 2020. Fracture-mediated deep seawater flow and mantle hydration on oceanic transform faults. Earth Planet. Sci. Lett. 532, 115988. https://doi.org/10.1016/j.epsl.2019.115988.
Regelous, M., Weinzierl, C.G., Haase, K.M., 2016. Controls on melting at spreading ridges from correlated abyssal peridotite–mid-ocean ridge basalt compositions. Earth Planet. Sci. Lett. 449, 1–11.
Roland, E., Lizarralde, D., McGuire, J.J., Collins, J.A., 2012. Seismic velocity constraints on the material properties that control earthquake behavior at the Quebrada-Discovery-Gofar transform faults, East Pacific Rise. J. Geophys. Res. Solid Earth 117.
Rouméjon, S., 2014. Serpentinisation des péridotites exhumées aux dorsales lentes : approches microstructurale, minéralogique et géochimique.
Rouméjon, S., Cannat, M., Agrinier, P., Godard, M., Andreani, M., 2014. Serpentinization and fluid pathways in tectonically exhumed peridotites from the southwest Indian ridge (62-65°E). J. Petrol. 56, 703–734. https://doi.org/10.1093/petrology/egv014.
Rouméjon, S., Williams, M.J., Früh-Green, G.L., 2018. In-situ oxygen isotope analyses in serpentine minerals: Constraints on serpentinization during tectonic exhumation at slow-and ultraslow-spreading ridges. Lithos 323, 156–173.
Rouméjon, S., Andreani, M., Früh-Green, G.L., 2019. Antigorite crystallization during oceanic retrograde serpentinization of abyssal peridotites. Contrib. Mineral. Petrol. 174, 1–25.
Rouxel, O., Dobbek, N., Ludden, J., Fouquet, Y., 2003. Iron isotope fractionation during oceanic crust alteration. Chem. Geol. 202, 155–182. https://doi.org/10.1016/j.chemgeo.2003.08.011.
Rüpke, L.H., Schmid, D.W., Perez-Gussinye, M., Hartz, E., 2013. Interrelation between rifting, faulting, sedimentation, and mantle serpentinization during continental margin formation—including examples from the Norwegian Sea. Geochem. Geophys. Geosyst. 14, 4351–4369.
Salters, V.J.M., Stracke, A., 2004. Composition of the depleted mantle. Geochem. Geophys. Geosyst. 5 https://doi.org/10.1029/2003GC000597.
Sauter, D., Cannat, M., 2010. The ultraslow spreading Southwest Indian ridge. Divers. Hydrothermal Syst. Slow Spreading Ocean Ridges 88, 153–173.
Sauter, D., Cannat, M., Rouméjon, S., Andreani, M., Birot, D., Bronner, A., Brunelli, D., Carlut, J., Delacour, A., Guyader, V., et al., 2013. Continuous exhumation of mantle-derived rocks at the Southwest Indian Ridge for 11 million years. Nat. Geosci. 6, 314–320.
Savage, P.S., Moynier, F., Chen, H., Shofner, G., Siebert, J., Badro, J., Puchtel, I.S., 2015. Copper isotope evidence for large-scale sulphide fractionation during Earth's differentiation. Geochem. Perspect. Lett 1, 53–64.
Savov, I., Guggino, S., Ryan, J.G., Fryer, P., Mottl, M.J., 2005a. Geochemistry of serpentine muds and metamorphic rocks from the Mariana Forearc, ODP Sites 1200 and 778-779, South Chamorro and Conical seamounts. Proc. Ocean Drill. Program Sci. Results 195, 1–49.
Savov, I., Ryan, J.G., D'Antonio, M., Kelley, K., Mattie, P., 2005b. Geochemistry of serpentinized peridotites from the Mariana Forearc Conical Seamount, ODP Leg 125: Implications for the elemental recycling at subduction zones. Geochem. Geophys. Geosyst. 6, 1–24. https://doi.org/10.1029/2004GC000777.
Savov, I., Ryan, J.G., D'Antonio, M., Fryer, P., 2007. Shallow slab fluid release across and along the Mariana arc-basin system: Insights from geochemistry of serpentinized peridotites from the Mariana fore arc. J. Geophys. Res. Solid Earth 112. https://doi.org/10.1029/2006JB004749.
Scambelluri, M., Tonarini, S., 2012. Boron isotope evidence for shallow fluid transfer across subduction zones by serpentinized mantle. Geology 40, 907–910.
Scambelluri, M., Cannao, E., Gilio, M., 2019. The water and fluid-mobile element cycles during serpentinite subduction. A review. Eur. J. Mineral. 31, 405–428. https://doi.org/10.1127/ejm/2019/0031-2842.
Schwarzenbach, E.M., Früh-Green, G.L., Bernasconi, S.M., Alt, J.C., Shanks III, W.C., Gaggero, L., Crispini, L., 2012. Sulfur geochemistry of peridotite-hosted hydrothermal systems : comparing the Ligurian ophiolites with oceanic serpentinites. Geochim. Cosmochim. Acta 91, 283–305. https://doi.org/10.1016/j.gca.2012.05.021.
Schwarzenbach, E.M., Früh-Green, G.L., Bernasconi, S.M., Alt, J.C., Plas, A., 2013. Serpentinization and carbon sequestration: a study of two ancient peridotite-hosted hydrothermal systems. Chem. Geol. 351, 115–133. https://doi.org/10.1016/j.chemgeo.2013.05.016.
Schwarzenbach, E.M., Vogel, M., Früh-Green, G.L., Boschi, C., 2021. Serpentinization, carbonation, and metasomatism of ultramafic sequences in the Northern Apennine Ophiolite (NW Italy). J. Geophys. Res. Solid Earth 126, e2020JB020619.
Scott, S.R., Sims, K.W.W., Frost, B.R., Kelemen, P.B., Evans, K.A., Swapp, S.M., 2017. On the hydration of olivine in ultramafic rocks: Implications from Fe isotopes in serpentinites. Geochim. Cosmochim. Acta 215, 105–121. https://doi.org/10.1016/j.gca.2017.07.011.
Searle, R.C., Escartín, J., 2004. The rheology and morphology of oceanic lithosphere and mid-ocean ridges. In: Mid-Ocean Ridges. American Geophysical Union (AGU), pp. 63–93. https://doi.org/10.1029/148GM03.
Seifert, K., Brunotte, D., 1996. Geochemistry of serpentinized mantle peridotite from Site 897 in the Iberia Abyssal Plain. Proc. Ocean Drill. Program 149. https://doi.org/10.2973/odp.proc.sr.149.216.1996. Sci. Results 149.
Seyfried Jr., W.E., Foustoukos, D.I., Fu, Q., 2007. Redox evolution and mass transfer during serpentinization: an experimental and theoretical study at 200 C, 500 bar with implications for ultramafic-hosted hydrothermal systems at Mid-Ocean Ridges. Geochim. Cosmochim. Acta 71, 3872–3886.
Sforna, M.C., Brunelli, D., Pisapia, C., Pasini, V., Malferrari, D., Ménez, B., 2018. Abiotic formation of condensed carbonaceous matter in the hydrating oceanic crust. Nat. Commun. 9, 5049. https://doi.org/10.1038/s41467-018-07385-6.
Snow, J., Dick, J., 1995. Pervasive magnesium loss by marine weathering of peridotite. Geochim. Cosmochim. Acta 59, 4219–4235.
Sossi, P.A., O'Neill, H.S.C., 2017. The effect of bonding environment on iron isotope fractionation between minerals at high temperature. Geochim. Cosmochim. Acta 196, 121–143. https://doi.org/10.1016/j.gca.2016.09.017.
Sossi, P.A., Halverson, G.P., Nebel, O., Eggins, S.M., 2015. Combined separation of Cu, Fe and Zn from rock matrices and improved analytical protocols for stable isotope determination. Geostand. Geoanal. Res. 39, 129–149. https://doi.org/10.1111/j.1751-908X.2014.00298.x.
Sossi, P.A., Nebel, O., Foden, J., 2016. Iron isotope systematics in planetary reservoirs. Earth Planet. Sci. Lett. 1, 1–14. https://doi.org/10.1016/j.epsl.2016.07.032.

Sossi, P.A., Nebel, O., O'Neill, H.S.C., Moynier, F., 2018. Zinc isotope composition of the Earth and its behaviour during planetary accretion. Chem. Geol. 477, 73–84. https://doi.org/10.1016/j.chemgeo.2017.12.006.

Szilas, K., Kelemen, P.B., Rosing, M.T., 2015. The petrogenesis of ultramafic rocks in the> 3.7 Ga Isua supracrustal belt, southern West Greenland: Geochemical evidence for two distinct magmatic cumulate trends. Gondwana Res. 28, 565–580.

Szitkar, F., Dyment, J., Choi, Y., Fouquet, Y., 2014. What causes low magnetization at basalt-hosted hydrothermal sites? Insights from inactive site Krasnov (MAR 16° 38′ N). Geochem. Geophys. Geosyst. 15, 1441–1451.

Ternieten, L., Früh-Green, G.L., Bernasconi, S.M., 2021. Distribution and sources of carbon in serpentinized mantle peridotites at the Atlantis Massif (IODP Expedition 357). J. Geophys. Res. Solid Earth 126, e2021JB021973.

Tichadou, C., Godard, M., Muñoz, M., Labaume, P., Vauchez, A., Gaucher, E.C., Calassou, S., 2021. Mineralogical and geochemical study of serpentinized peridotites from the North-Western Pyrenees: New insights on serpentinization along magma-poor continental passive margins. Lithos 406, 106521.

Toffolo, L., Nimis, P., Martin, S., Tumiati, S., Bach, W., 2017. The Cogne magnetite deposit (Western Alps, Italy): a late Jurassic seafloor ultramafic-hosted hydrothermal system? Ore Geol. Rev. 83, 103–126.

Tucholke, B.E., Lin, J., Kleinrock, M.C., 1998. Megamullions and mullion structure defining oceanic metamorphic core complexes on the Mid-Atlantic Ridge. J. Geophys. Res. Solid Earth 103, 9857–9866.

Tucholke, B.E., Behn, M.D., Buck, W.R., Lin, J., 2008. Role of melt supply in oceanic detachment faulting and formation of megamullions. Geology 36, 455–458.

Turekian, K.K., 1968. Oceans, Foundation. ed. Prentice-Hall, New York.

Ulmer, P., Trommsdorff, V., 1995. Serpentine stability to mantle depths and subduction-related magmatism. Science (80-.). 268, 858–861. https://doi.org/10.1126/science.268.5212.858.

Vils, F., Pelletier, L., Kalt, A., Müntener, O., Ludwig, T., 2008. The Lithium, Boron and Beryllium content of serpentinized peridotites from ODP Leg 209 (Sites 1272A and 1274A): Implications for lithium and boron budgets of oceanic lithosphere. Geochim. Cosmochim. Acta 72, 5475–5504. https://doi.org/10.1016/j.gca.2008.08.005.

Vils, F., Tonarini, S., Kalt, A., Seitz, H.M., 2009. Boron, lithium and strontium isotopes as tracers of seawater-serpentinite interaction at Mid-Atlantic ridge, ODP Leg 209. Earth Planet. Sci. Lett. 286, 414–425. https://doi.org/10.1016/j.epsl.2009.07.005.

Wang, Z.Z., Liu, S.A., Liu, J., Huang, J., Xiao, Y., Chu, Z.Y., Zhao, X.M., Tang, L., 2017. Zinc isotope fractionation during mantle melting and constraints on the Zn isotope composition of Earth's upper mantle. Geochim. Cosmochim. Acta 198, 151–167. https://doi.org/10.1016/j.gca.2016.11.014.

Warren, J.M., 2016. Global variations in abyssal peridotite compositions. Lithos 248–251, 193–219. https://doi.org/10.1016/j.lithos.2015.12.023.

Whattam, S.A., Früh-Green, G.L., Cannat, M., De Hoog, J.C.M., Schwarzenbach, E.M., Escartin, J., John, B.E., Leybourne, M.I., Williams, M.J., Rouméjon, S., Akizawa, N., Boschi, C., Harris, M., Wenzel, K., McCaig, A., Weis, D., Bilenker, L., 2022. Geochemistry of serpentinized and multiphase altered Atlantis Massif peridotites (IODP Expedition 357): Petrogenesis and discrimination of melt-rock vs. fluid-rock processes. Chem. Geol. 594, 120681 https://doi.org/10.1016/j.chemgeo.2021.120681.

Williams, H.M., Bizimis, M., 2014. Iron isotope tracing of mantle heterogeneity within the source regions of oceanic basalts. Earth Planet. Sci. Lett. 404, 396–407. https://doi.org/10.1016/j.epsl.2014.07.033.

Williams, H.M., McCammon, C.A., Peslier, A.H., Halliday, A.N., Teutsch, N., Levasseur, S., Burg, J.P., 2004. Iron isotope fractionation and the oxygen fugacity of the mantle. Science (80-.). 304, 1656–1659. https://doi.org/10.1126/science.1095679.

Zeng, Z., Wang, Q., Wang, X., Chen, S., Yin, X., Li, Z., 2012. Geochemistry of abyssal peridotites from the super slow-spreading Southwest Indian Ridge near 65°E: Implications for magma source and seawater alteration. J. Earth Syst. Sci. 121, 1317–1336. https://doi.org/10.1007/s12040-012-0229-z.

Zeng, Z., Ma, Y., Yin, X., Selby, D., Kong, F., Chen, S., 2015. Factors affecting the rare earth element compositions in massive sulfides from deep-sea hydrothermal systems. Geochem. Geophys. Geosyst. 16, 2679–2693.

Zhang, Y., Gazel, E., Gaetani, G.A., Klein, F., 2021. Serpentinite-derived slab fluids control the oxidation state of the subarc mantle. Sci. Adv. 7, 1–8. https://doi.org/10.1126/sciadv.abj2515.